



ELSEVIER

Contents lists available at SciVerse ScienceDirect

## International Journal of Plasticity

journal homepage: [www.elsevier.com/locate/ijplas](http://www.elsevier.com/locate/ijplas)

# Micromechanical analysis of strain rate-dependent deformation and failure in composite microstructures under dynamic loading conditions

Yuli Chen<sup>b,1</sup>, Somnath Ghosh<sup>a,\*,2,3</sup>

<sup>a</sup> Department of Civil and Mechanical Engineering, Johns Hopkins University, Baltimore, MD 21218, USA

<sup>b</sup> Institute of Solid Mechanics, Beihang University (BUAA), Beijing 100191, PR China

## ARTICLE INFO

### Article history:

Received 7 April 2011

Received in final revised form 7 August 2011

Available online xxxx

### Keywords:

D. Energy absorption

D. Energy dissipation

D. High strain rate

D. Failure mode

A. Fiber-reinforced composites

## ABSTRACT

This paper is intended to study the effect of microstructural morphology and loading characteristics on micromechanical stress-wave propagation leading to different damage mechanisms, energy absorption and dissipation characteristics. The composite material microstructure is represented by brittle fibers in a ductile matrix in different arrangements. The matrix material behavior is modeled using a strain-rate dependent elastic-viscoplastic constitutive model with damage evolution based on the Gurson–Tvergaard–Needleman model with a Johnson–Cook type hardening law. Damage in the fiber is modeled by an isotropic continuum damage mechanics (CDM) model. The microstructural failure modes and energy absorption and dissipation properties show strong dependence on the load types, volume fractions and microstructures, with relatively lower dependence on strain rates. The studies show that for the SiC fiber/Al7075-T6 composites, the microstructures with 15–20% unidirectional hexagonal arrangement of fibers are good designs for energy absorption and dissipation.

© 2011 Elsevier Ltd. All rights reserved.

## 1. Introduction

Understanding the mechanical behavior of composite materials at strain rates in excess of  $10^3 \text{ s}^{-1}$  is important for a wide variety of applications, especially in the military and automotive industries. Strain rates in this range are experienced in vehicle crashworthiness as well as in armor penetration and blast conditions e.g. with improvised explosive devices. The recent years have seen a surge in research on material and structural response subject to high strain rate loading. Jacinto et al. (2001) and Langdon et al. (2005) have conducted experimental and numerical investigations on the response of metallic plates subjected to explosive loads. Mamalis et al. (2005) have compared the crushing response and crashworthiness characteristics of thin-walled fiber reinforced plastic tubes at high compressive strain rates to their static response. They identified three modes of brittle collapse to be functions of strain rate, laminate construction and tube geometry.

A number of experimental studies have been conducted for understanding the high strain rate dynamic deformation behavior of metals, ceramics, and composites. Extensive systematic studies have been conducted by Khan et al. on the dynamic response of metals (Khan and Liang, 1999; Liang and Khan, 2000), alloys (Khan et al., 2004, 2007a,b; Khan and Baig, 2011), and polymers (Khan and Farrokh, 2006; Farrokh and Khan, 2010), under uniaxial and multiaxial loadings, over wide ranges of strain rates and temperatures. They have also investigated influence factors in ultra-fine grained and nanocrystalline Cu and Al, including the effects of grain size, strain rate, and temperature (Farrokh and Khan, 2009). Phenomenological

\* Corresponding author. Tel.: +1 410 516 7833; fax: +1 410 516 7473.

E-mail address: [sghosh20@jhu.edu](mailto:sghosh20@jhu.edu) (S. Ghosh).

<sup>1</sup> Previously Post-doctoral Researcher in the Department of Mechanical Engineering, The Ohio State University, OH 43210, USA.

<sup>2</sup> Previously Professor in the Department of Mechanical Engineering, The Ohio State University, OH 43210, USA.

<sup>3</sup> M.G. Callas Professor.

constitutive models have been proposed based on these comprehensive experimental studies, including the KHL model (Khan and Liang, 1999) and the KLF model (Farrokh and Khan, 2009). The compressive response of metals has been studied in (Nemat-Nasser et al., 2005a,b; Nemat-Nasser and Choi, 2005). Porous NiTi shape-memory alloys have been investigated at different strain rates in (Nemat-Nasser et al., 2005c), where the transition stress for stress-induced martensite formation is found to reach the yield stress of the austenite phase at a critical strain-rate level. This suggests two different micromechanisms of deformation of this alloy under high and low strain rates. Valiev et al. (1997) have observed high strain rate superplasticity in commercial aluminum alloys with ultrafine grain sizes and have reported different stress–strain behavior at different strain rates. Benallal et al. (2008) have investigated negative strain-rate sensitivity in the aluminum alloy AA5083, a phenomenon that has been also observed in recent room temperature experimental studies on the aluminum alloy AA5182-O by Khan and Baig (2011). Brar et al. (2009) have studied the mechanical response of Aluminum 7075-T651 and 7075-T6 alloys at quasi-static and high strain rates and have inferred that while strength does not show much variation, the fracture properties do exhibit a large variation with strain rates. Meyers et al. (1995) have experimentally observed similar response of copper at low- and high-strain-rates. Grain-size is found to have a profound effect on the mechanical response suggesting the dependence of shock response on the microstructure. For ceramics, Kanel et al. (2009) have discussed three different experimental configurations, a layered target assembly, a pre-stressed target plate, and a convex flyer plate, for diagnosing the modes of inelastic deformation and evaluating the failure thresholds at shock compression. Various high strain rate studies have been conducted for composite materials as well. Experimental studies include those by Kumar and Garg (1988), who have tested unidirectional glass–epoxy composite under dynamic compressive loading conditions to study the effect of fiber orientations on failure modes. They have found that fiber orientations have significant influence on the failure modes. Oguni and Ravichandran (2001) have examined rate dependent behavior in their experiments on E-glass/vinylester composites, showing that the compressive strength increases with strain rate.

A number of theoretical and numerical models have also been developed on high strain-rate material deformation and failure response. For metals, well known models that are currently used include the Johnson and Cook (1983) model, Steinberg–Cochran–Guinan–Lund model (Steinberg et al., 1980; Steinberg and Lund, 1988), Zerilli and Armstrong (1987) model, mechanical threshold-stress model by Follansbee and Kocks (1988), Preston et al. (2003) model, the nonlocal gradient-enhanced visco-inelasticity model (Abu Al-Rub and Voyiadjis, 2006; Voyiadjis and Abu Al-Rub, 2006), as well as the KHL model (Khan and Liang, 1999) and KLF model (Farrokh and Khan, 2009), among others. For modeling high strain rate behavior of composites, Zhou et al. (2005) have combined the shear-lag model and Monte Carlo simulation technique to simulate high strain rate tensile failure process of unidirectional SiC fiber-reinforced metal-matrix composites. Batra and Hassan (2007) have developed a three-dimensional finite element model with rate-dependent damage evolution equations to ascertain damage due to fiber/matrix debonding, fiber breakage, matrix cracking, and delamination in fiber-reinforced composites in underwater explosions. Recently Brüning and Gerke (2011) have developed a set of constitutive equations for large rate-dependent elastic–plastic–damage materials. This model is based on the concepts of continuum damage mechanics, and is able to analyze adiabatic, high strain rate dependent deformation processes for a wide range of stress triaxialities. For polycrystalline metals and alloys subjected to very high rates of deformation ( $10^4$ – $10^8$  s<sup>-1</sup>), Austin and McDowell (2011) have developed a physically-based model based on physical descriptions of slip resistance and the plastic flow rate, where mobile and immobile dislocation densities are assigned as path dependent internal state variables.

The present paper is aimed at developing a three-dimensional finite deformation computational model for investigating the microstructural mechanisms of deformation and damage in fiber-reinforced metal-matrix composites subjected to high strain rate loading conditions  $\sim 10^3$ – $10^5$  s<sup>-1</sup>. The microstructures considered, consist of an elastic fiber phase that undergoes brittle damage and a rate-dependent plastic matrix phase that is assumed to undergo ductile failure by nucleation, growth and coalescence of microscopic voids. Brittle damage in the fiber is modeled by a scalar continuum damage mechanics (CDM) model, while ductile fracture in the matrix is modeled by the Gurson, Tvergaard and Needleman or GTN model (Gurson, 1977; Tvergaard, 1990; Chu and Needleman, 1980; Tvergaard and Needleman, 1984) that accounts for damage accumulation due to shearing in (Nahshon and Hutchinson, 2008; Nahshon and Xue, 2009; Xue et al., 2010). The GTN model is augmented with a rate dependent plastic behavior for the pure matrix phase through the Johnson–Cook model (Johnson and Cook, 1983) representation that is widely used in high-strain-rate deformation of many metallic materials. A focus of this paper is on the effect of microstructural morphology and loading characteristics on micromechanical stress-wave propagation leading to different damage mechanisms. The study also has important implications in the energy absorption and dissipation at high strain rates. The paper begins with a development of the micro-mechanical model, including the representative volume element (RVE) model with associated boundary conditions, the constitutive models for both the fiber and the matrix phases, and its numerical implementation. Simulations are subsequently done to investigate the damage and failure mechanisms as well as the influence factors on the failure modes and the ability of energy absorption and dissipation.

## 2. Model of the microstructural representative volume element

The microstructural representative volume element (RVE), a small micro-region for which the volume average of variables are the same as those for the entire body (Drugan and Willis, 1996; Kouznetsova et al., 2002; Kanit et al., 2003; Khan et al., 2004; Peng et al., 2008; Jain and Ghosh, 2009), is essential for the determination of effective material properties by homogenization. It generally depends on the material property of interest and can vary significantly from one class of

properties to another (Swaminathan et al., 2006; Swaminathan and Ghosh, 2006). Conventionally, studies have been conducted with the RVE represented by a unit cell consisting of a single heterogeneity in a uniform matrix as shown in Fig. 1 e.g. (Lee and Mal, 1998; Jain and Ghosh, 2009). The underlying assumptions are that the microstructure depicts a uniform, periodically repetitive array of heterogeneities and the body is subjected to homogeneous boundary conditions.

### 2.1. The RVE domain and boundary conditions

In the present problem, the RVE is represented by a periodic unit cell as shown in Fig. 1(b), which includes an elastic brittle fiber in a porous ductile metal matrix. To test the validity of assuming a periodic unit cell as a RVE for dynamic problems, two microscopic domains are simulated under dynamic conditions as shown in Fig. 2(a). The larger microstructural domain is created by translating the RVE in the  $x$ - and  $y$ -directions to yield resulting in an ensemble of 9 unit cells. The constitutive models and the material parameters for the constituent materials are described in the subsequent sections. Periodic boundary conditions are applied on both the single unit cell and the larger domain by constraining nodes on opposite faces of the RVE boundary. Four loading cases with applied macroscopic rate of deformation  $\bar{D}$  are considered as follows:

Case 1:  $\bar{D}_{22} = 5000 \text{ s}^{-1}$ , all other components = 0.0;

Case 2:  $\bar{D}_{12} = \bar{D}_{21} = 5000 \text{ s}^{-1}$ , all other components = 0.0;

Case 3:  $\bar{D}_{22} = 50,000 \text{ s}^{-1}$ , all other components = 0.0;

Case 4:  $\bar{D}_{12} = \bar{D}_{21} = 50,000 \text{ s}^{-1}$ , all other components = 0.0.

The macroscopic strain increment is applied on the RVE in each time increment by decomposing the displacement increment on the boundary into a macroscopic averaged and a periodic part as discussed by Pellegrino et al. (1999) and Segurado and Llorca (2002), i.e.

$$\Delta U_i = \Delta E_{ij} X_j + \Delta \tilde{U}_i \quad (1)$$

where  $\Delta E_{ij} = \bar{D}_{ij} \Delta t$  is the macroscopic strain increment. Since the periodic part  $\Delta \tilde{U}_i$  is equal on corresponding nodes of opposite faces of the RVE (say  $n_1^p$  and  $n_2^p$ ), the total displacement at these nodes are related as:

$$(\Delta U_i)_{n_2^p} - (\Delta U_i)_{n_1^p} = \Delta E_{ij} \Delta X_j \quad (2)$$

where  $\Delta X_i$  are the relative coordinates of nodes on opposite faces. Macroscopic strains are then applied, in conjunction with the periodicity constraints. Details of implementation in commercial software for the dynamic simulations is given by Wu and Koishi (2009).

Results are compared for the two micro-domains considered under identical conditions. The relative error in any chosen variable is defined as the absolute value of the difference between the corresponding values in the two domains divided by the value in the larger domain, i.e.  $Err_v = \|V_{1 \text{ unit cell}} - V_{9 \text{ unit cells}}\| / \|V_{9 \text{ unit cells}}\|$ . Values of both global and local (at the geometric center) relative error  $Err_v$  in the von Mises stress and the maximum principal stress are shown in Table 1. In most cases the relative error decreases with increasing the true strain from 10% to 20%, since it is mainly caused by stress wave

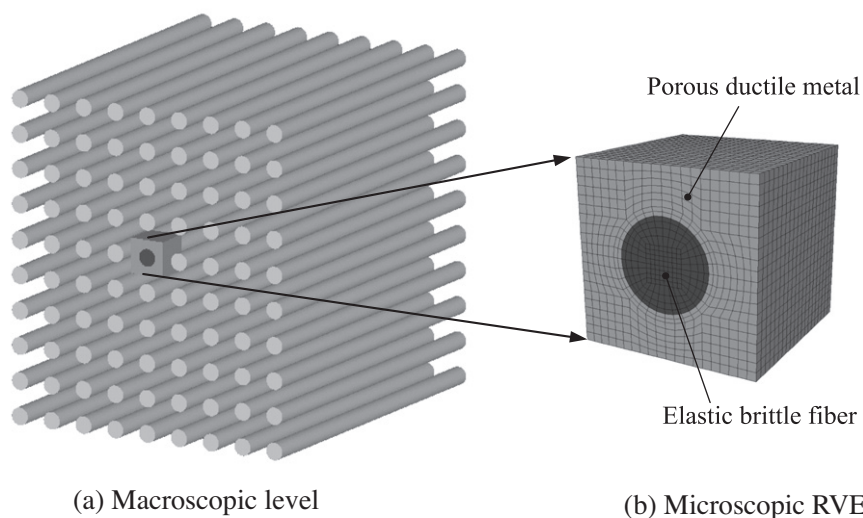


**Fig. 1.** Schematic diagram of the analysis model: (a) overall composite microstructure with a square array of unidirectional cylindrical fibers and (b) microstructural representative volume element (RVE).

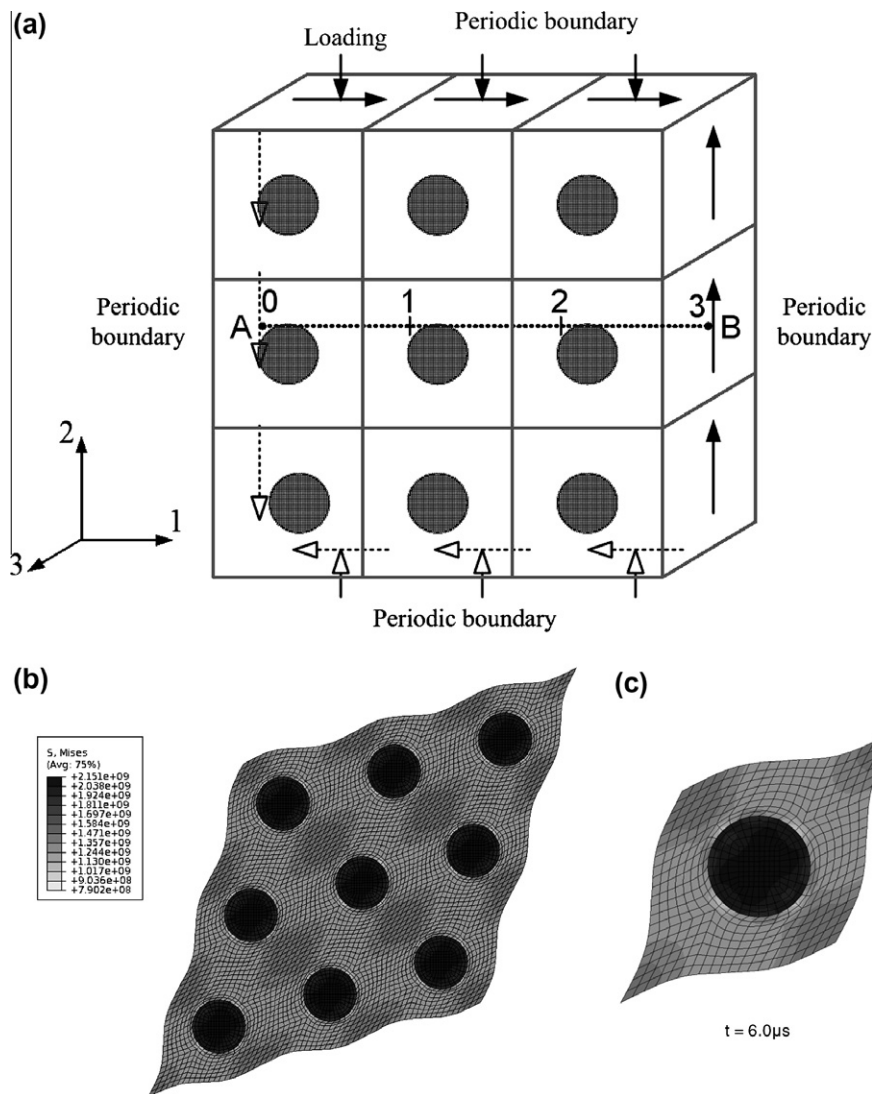


**Fig. 2.** Establishing the RVE by comparing unit cell results with those from a larger ensemble with 9 unit cells: (a) the model with 9 unit cells; (b) stress distribution and deformation of the 9-unit-cell model under shear loading; and (c) stress distribution and deformation of the single unit cell under shear loading.

**Table 1**

Relative errors  $Err_V$  in the von Mises stress (V.M.) and the maximum principal stress (M.P.) for a single unit-cell and 9-unit-cell models.

Case no.	Error in averaged stress (%)				Error in local stress at geometric center (%)			
	True strain = 10%		True strain = 20%		True strain = 10%		True strain = 20%	
	V.M.	M.P.	V.M.	M.P.	V.M.	M.P.	V.M.	M.P.
1	0.01	0.02	0.01	0.02	0.03	0.02	0.02	0.01
2	0.00	0.00	0.00	0.00	0.02	0.02	0.01	0.00
3	3.19	2.70	0.13	0.90	6.31	0.93	1.15	4.26
4	0.23	0.13	0.14	0.05	5.95	5.41	0.60	1.54

propagation from the boundary to the interior of the model. At the initial stages a high error is seen since the stress level is low and the stress wave has not reached the center. However with the increase of strain, the stress level of the entire model increases and the error becomes low in comparison with the higher stress level. Comparing the loading cases 1 and 3, and 2 and 4, it is seen that the error decreases with the decrease of the strain rate. At lower strain rates, the stress wave has more time to propagate in the interior, which means the difference caused by the size of the model becomes smaller. Although the

relative error shows an increasing trend with higher strain rates, Table 1 illustrates that the relative error is less than 7% for strain rates up to  $\sim 10^5 \text{ s}^{-1}$ . This error is considered to be acceptable for the range of strain rates investigated in this paper ( $\sim 10^3$ – $10^5 \text{ s}^{-1}$ ) and hence a single unit cell is used.

The deformation profiles and stress distributions for the higher strain rates with larger relative errors are shown in Fig. 2. The von Mises stress along section AB in Fig. 2(a) is presented in Fig. 3(a) and (b) for loading cases 3 and 4 respectively. Figs. 2 and 3 again demonstrate that the differences in deformation and stress distributions between the single unit cell and the larger micro-domain are within acceptable tolerances. Hence, the single unit cell with periodic boundary condition is henceforth adopted for the study of the high strain rate problems.

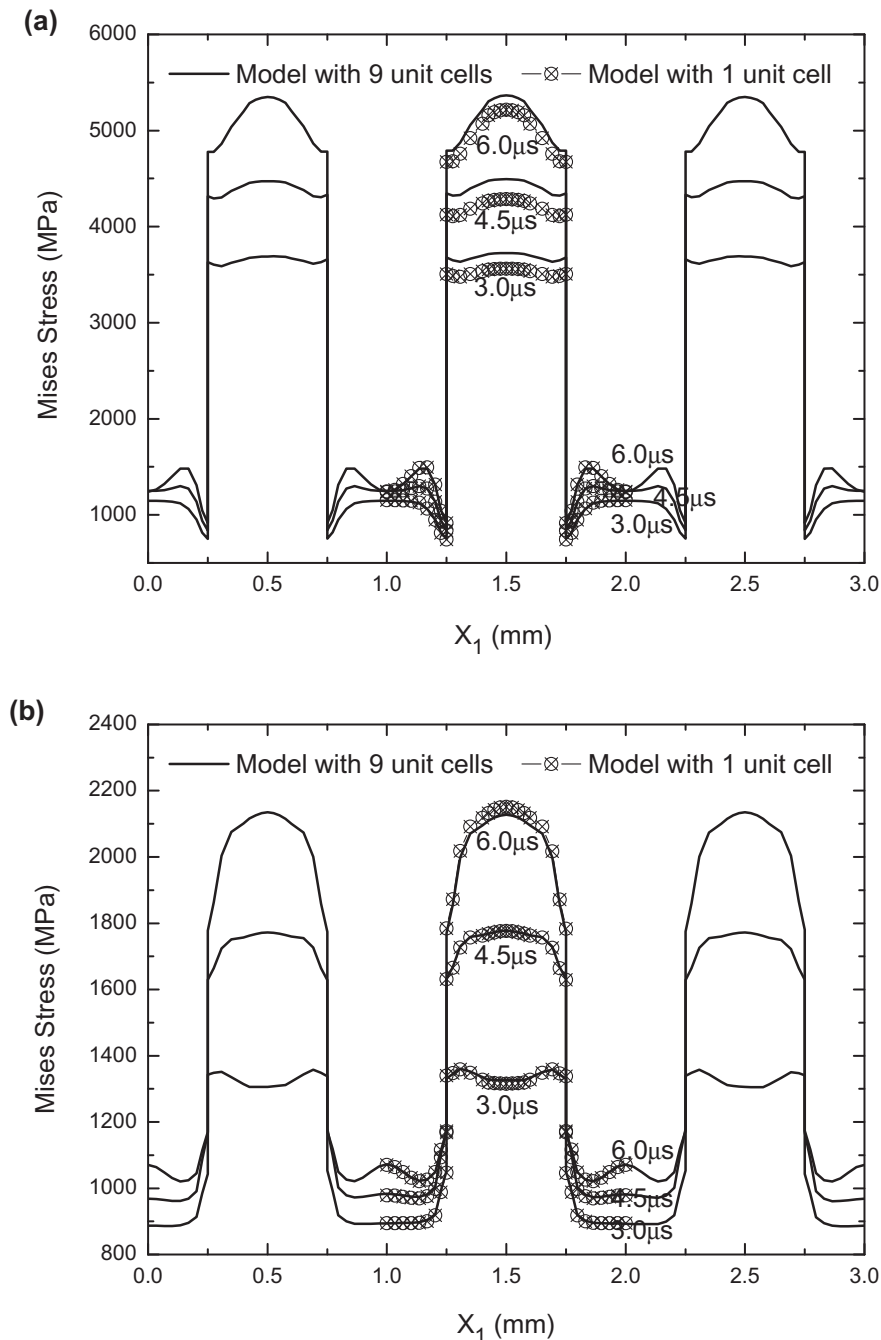


**Fig. 3.** Comparing von Mises stress distribution in the unit cell with those in a larger ensemble with 9 unit cells: (a) compressive loading and (b) shear loading.

## 2.2. Constitutive models

This section briefly discusses the constitutive and continuum damage models that are used to describe the deformation and damage response of fiber reinforced ductile matrix composites, consisting of fiber and the matrix phases. Their mechanical responses are modeled by two different sets of constitutive and damage models respectively. The interface between the matrix and fiber phases is assumed to be coherent with no explicit debonding.

### 2.2.1. Fiber phase model

The mechanical behavior of the hard and brittle fiber is characterized by high stiffness and strength and low failure strain. For example, the tensile strength for silicon carbide (SiC) fibers is typically of the order of 6 GPa with a failure strain of approximately 1.4%. The failure process is short and the stress drops very suddenly at the inception of brittle fracture. The brittle fiber is assumed to be isotropic, elastic undergoing small deformation, but finite rotation. The stress–strain relation in a rotated system is given as:

$$\boldsymbol{\sigma} = \mathbf{C} : \boldsymbol{\varepsilon} \quad (3)$$

in which  $\mathbf{C}$  is the fourth order isotropic secant stiffness tensor as

$$C_{ijkl} = 2G\delta_{ik}\delta_{jl} + \left(K - \frac{2}{3}G\right)\delta_{ij}\delta_{kl} \quad (4)$$

where  $G = E/[2(1 + \nu)]$  and  $K = E/[3(1 - 2\nu)]$  are the shear and bulk moduli, depending only on the stiffness  $E$  and Poisson's ratio  $\nu$ . Fiber damage is modeled using a continuum damage mechanics (CDM) model proposed in (Kachanov, 1958; Simo and Ju, 1987; Chaboche, 1988; Jain and Ghosh, 2009), in which the elastic stiffness reduces with increasing deformation induced damage. From elastic energy equivalence, which assumes that the elastic complementary energy in a damaged material with the actual stress is equal to that in a hypothetical material with a fictitious effective stress, the relation between the damaged and undamaged elastic stiffness for an isotropic material may be established as

$$E = (1 - D)^2 E^0 \quad (5)$$

where  $D$  represents the damage, and  $E$  and  $E^0$  are elastic modulus in the damaged and undamaged state respectively. For the brittle materials in the absence of plasticity, the damage variable is assumed to evolve following a damage evolution law (Lemaitre and Chaboche, 1990) as:

$$\dot{D} = \begin{cases} (\bar{\varepsilon}/\varepsilon_0)^{S^*} \dot{\bar{\varepsilon}} & \text{when } \bar{\varepsilon} \geq \varepsilon_D \text{ and } \dot{\bar{\varepsilon}} > 0 \\ 0 & \text{when } \bar{\varepsilon} < \varepsilon_D \text{ or } \dot{\bar{\varepsilon}} \leq 0 \end{cases} \quad (6)$$

where  $\bar{\varepsilon} = \sqrt{2\varepsilon_{ij}\varepsilon_{ij}/3}$  is the equivalent strain,  $\varepsilon_D$  is a variable threshold of equivalent strain, and  $\varepsilon_0$  and  $S^*$  are constant material parameters calibrated from experimental results. The first in Eq. (6) indicates that the damage increases when (i) the equivalent strain is at or beyond the damage surface i.e.  $\bar{\varepsilon} \geq \varepsilon_D$  and (ii) the rate of equivalent strain is positive i.e.  $\dot{\bar{\varepsilon}} > 0$ . Thus the elastic modulus degrades during loading. Unloading is characterized by the second in Eq. (6), when the equivalent strain is inside the damage surface i.e.  $\bar{\varepsilon} < \varepsilon_D$  and the equivalent strain rate is not positive i.e.  $\dot{\bar{\varepsilon}} \leq 0$ . In this case, there is no change in damage or elastic modulus. The stress–strain response for the loading–unloading process is depicted in Fig. 4. During loading, the stress initially increases with increasing strain prior to the occurrence of damage. It then decreases to zero value with increasing damage. If unloading happens prior to the commencement of damage, e.g. at point 1 in Fig. 4, the stress–strain

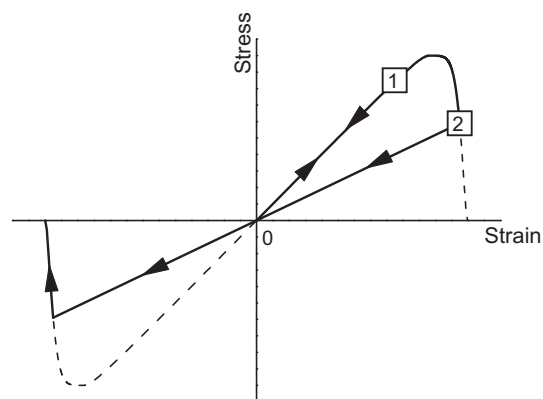


**Fig. 4.** Schematic stress–strain response curve for the loading–unloading process for the isotropic continuum damage mechanics (CDM) model of fiber failure.

curve retraces its original path. If unloading occurs during the damage phase, e.g. at point 2 in Fig. 4, the stress–strain curve goes approaches the origin with a constant damaged elastic modulus. For transitioning from tension to compression, the curve continues in the reverse direction with the same constant elastic modulus until the equivalent strain reaches the damage surface. Subsequently, the damage increases and elastic modulus decreases as shown in Fig. 4. For complete damage, the stress reduces to zero indicating loss of load carrying capacity.

### 2.2.2. Matrix phase model

Ductile metals are used as the matrix phase in composites for their good energy absorption properties. The matrix phase in this study is assumed to undergo rate-dependent elasto-plastic deformation and ductile failure due to nucleation, growth and coalescence of microscopic voids (Tvergaard, 1990). The matrix material is modeled using finite deformation constitutive relations for strain-rate-dependent porous plasticity with microscopic voids in a rotated framework (Green and Naghdi, 1965; Ghosh and Kikuchi, 1991). In this formulation, the constitutive relations are expressed in a rotated Lagrangian system in terms of the rotated Cauchy stress tensor  $\Delta\sigma_R = \mathbf{R}^T \Delta\sigma \mathbf{R}$  and the rotated rate of deformation tensor  $\mathbf{D}_R = \mathbf{R}^T \mathbf{D} \mathbf{R}$ , where  $\mathbf{R}$  is a proper orthogonal tensor representing a pure rotation obtained from the polar  $\mathbf{F} = \mathbf{R}\mathbf{U}$  decomposition of the deformation gradient tensor  $\mathbf{F} = \nabla_0 \mathbf{x}$ . The subscript 0 refers to the reference configuration. All the following equations are developed in a rotated Lagrangian system. The total strain rate is assumed to follow an additive decomposition into elastic and plastic parts as:

$$\mathbf{D}_R = \mathbf{D}_R^e + \mathbf{D}_R^p \quad (7)$$

Ductile fracture in metallic materials is governed by the mechanisms of microscopic void nucleation, growth and coalescence (Tvergaard, 1990). The most widely used model for ductile failure is the Gurson, Tvergaard and Needleman or GTN model (Gurson, 1977; Tvergaard, 1990; Chu and Needleman, 1980; Tvergaard and Needleman, 1984). It is a micromechanical model, in flow surface depends on the evolution of damage or porosity parameter  $f$  as well as on the hydrostatic stress. A variety of modifications have been made to the GTN model to extend its range of applications (Leblond et al., 1994; Besson et al., 2003; Wen et al., 2005; Nahshon and Hutchinson, 2008; Ghosh et al., 2009; Paquet and Ghosh, 2010). Hao and Brocks (1997) have established a constitutive law of ductile fracture for rate and temperature-dependent materials with isotropic and kinematic hardening by introducing two additional parameters to the GTN model, which account for the influences of strain rate, inertia and the average distance between voids. Recently Paquet and Ghosh (2010) have extended GTN model to rate-dependent porous elastic-viscoplastic model by using Perzyna's viscoplastic over-stress model. However, both these models are only suitable for low strain rate problems (less than  $10^{-1} \text{ s}^{-1}$ ).

The rate-dependent plastic behavior of the porous ductile matrix is governed by the GTN yield function (Gurson, 1977; Tvergaard, 1990; Chu and Needleman, 1980; Tvergaard and Needleman, 1984) in a rotated Lagrangian system as:

$$\phi(\bar{\sigma}_M) = \left(\frac{q_R}{\bar{\sigma}_M}\right)^2 + 2q_1 f^* \cosh\left(-\frac{3}{2} \frac{q_2 p_R}{\bar{\sigma}_M}\right) - (1 + q_3 f^{*2}) = 0 \quad (8)$$

where  $q_1, q_2, q_3$  are parameters related to void growth proposed in Tvergaard (1981, 1982),  $q_R = \sqrt{3\sigma'_r : \sigma'_r/2}$  and  $p_R = -\sigma_R : \mathbf{I}/3$  are the von Mises equivalent stress and the hydrostatic pressure respectively,  $\sigma'_r$  is the rotated Cauchy stress deviator,  $\bar{\sigma}_M$  is the yield stress of the undamaged matrix material. Subscript  $M$  is used to designate association with the pure underlying matrix without voids, and the acceleration function  $f^*$ , which accounts for rapid loss of stress carrying capacity due to void, is given by

$$f^* = \begin{cases} f & f \leq f_c \\ f_c + \frac{f_f - f_c}{f_f - f_c} (f - f_c) & f > f_c \end{cases} \quad (9)$$

Here  $f$  is the void volume fraction,  $f_c$  is a critical value for void coalescence,  $f_f$  is its value at failure and  $f_f^*$  is the value of  $f^*$  at failure.

The high strain rate response of the pure underlying matrix without voids is assumed to be governed by the rate-dependent hardening law (Johnson and Cook, 1983) given as:

$$\dot{\epsilon}_M^p = H[\phi(\sigma_0)] \dot{\epsilon}_0 \exp\left[\frac{\bar{\sigma}_M}{C\sigma_0(1 - \hat{\theta}^m)} - \frac{1}{C}\right] \quad (10)$$

where  $\dot{\epsilon}_M^p$  is the equivalent plastic strain rate,  $\sigma_0 = A + B(\dot{\epsilon}_M^p)^n$  is the material yield stress under static load, and  $A, B, C, m$  and  $n$  are material parameters that can be calibrated from experimental data.  $\dot{\epsilon}_0$  is a reference strain rate,  $\hat{\theta}$  is a normalized temperature, and  $H[x]$  is the Heaviside step function expressed as

$$H[x] = \begin{cases} 0 & x \leq 0 \\ 1 & x > 0 \end{cases} \quad (11)$$

The material plastic strain rate tensor is consequently expressed as

$$\dot{\epsilon}_M^p = \sqrt{\frac{3}{2}} H[\phi(\sigma_0)] \dot{\epsilon}_0 \exp\left[\frac{\bar{\sigma}_M}{C\sigma_0(1 - \hat{\theta}^m)} - \frac{1}{C}\right] \frac{\partial \phi / \partial \sigma_M}{\|\partial \phi / \partial \sigma_M\|} \quad (12)$$

Next for the porous matrix material, the overall plastic strain rate follows the associated flow rule as:

$$\mathbf{D}_R^p = \dot{\lambda} \frac{\partial \phi}{\partial \boldsymbol{\sigma}_R} \quad (13)$$

where  $\dot{\lambda}$  is a viscoplastic multiplier. The equivalence of the rate of dissipative energy yields

$$\boldsymbol{\sigma}_R : \mathbf{D}_R^p = (1-f) \bar{\boldsymbol{\sigma}}_M \dot{\bar{\boldsymbol{\varepsilon}}}_M^p \quad (14)$$

Substituting the flow rule (13) into the energy equivalence equation (14), the viscoplastic multiplier  $\dot{\lambda}$  can be obtained as

$$\dot{\lambda} = \frac{(1-f) \bar{\boldsymbol{\sigma}}_M H[\phi(\sigma_0)] \dot{\varepsilon}_0 \exp \left[ \frac{\bar{\boldsymbol{\sigma}}_M}{C(A+B(\bar{\boldsymbol{\varepsilon}}_M^p)^n)(1-\dot{\theta}^m)} - \frac{1}{C} \right]}{\boldsymbol{\sigma}_R : \frac{\partial \phi}{\partial \boldsymbol{\sigma}_R}} \quad (15)$$

Substituting Eq. (15) into Eq. (13) yields the overall plastic strain rate as:

$$\mathbf{D}_R^p = \frac{(1-f) \bar{\boldsymbol{\sigma}}_M H[\phi(\sigma_0)] \dot{\varepsilon}_0 \exp \left[ \frac{\bar{\boldsymbol{\sigma}}_M}{C(A+B(\bar{\boldsymbol{\varepsilon}}_M^p)^n)(1-\dot{\theta}^m)} - \frac{1}{C} \right]}{\boldsymbol{\sigma}_R : \frac{\partial \phi}{\partial \boldsymbol{\sigma}_R}} \frac{\partial \phi}{\partial \boldsymbol{\sigma}_R} \quad (16)$$

The evolution rate of the macroscopic void volume fraction  $f$  is additively decomposed into growth and nucleation parts (Chu and Needleman, 1980; Tvergaard and Needleman, 1984, 1995), as:

$$\dot{f} = \dot{f}_{\text{nucleation}} + \dot{f}_{\text{growth}} \quad (17)$$

The void nucleation rate is given as:

$$\dot{f}_{\text{nucleation}} = A(\bar{\boldsymbol{\varepsilon}}_M^p) \dot{\bar{\boldsymbol{\varepsilon}}}_M^p \quad (18)$$

where the parameter  $A$  is defined as a function of the matrix equivalent plastic strain  $\bar{\boldsymbol{\varepsilon}}_M^p$ , i.e.

$$A(\bar{\boldsymbol{\varepsilon}}_M^p) = \frac{f_N}{s_N \sqrt{2\pi}} \exp \left[ -\frac{1}{2} \left( \frac{\bar{\boldsymbol{\varepsilon}}_M^p - \varepsilon_N}{s_N} \right)^2 \right] \quad (19)$$

$f_N$  is the void volume fraction of nucleated voids,  $\varepsilon_N$  is the mean value of normal distribution of the nucleation strain, and  $s_N$  the distribution's standard deviation. It is assumed that voids are nucleated only in tension and no nucleation occurs in compression.

The matrix void growth rate is expressed as:

$$\dot{f}_{\text{growth}} = (1-f) \mathbf{D}_R^p : \mathbf{I} + k_{\omega} f \omega(\boldsymbol{\sigma}_R) \frac{\boldsymbol{\sigma}'_R : \mathbf{D}_R^p}{q_R} \quad (20)$$

The first term is due to the dilatation, while the second term is an amendment for the low stress triaxiality failure introduced by Nahshon and Hutchinson (2008). Here the coefficient  $k_{\omega}$  is a material parameter, specifying the magnitude of the damage growth rate in shear, and the invariant measure  $\omega(\boldsymbol{\sigma}_R)$  (Nahshon and Hutchinson, 2008; Nahshon and Xue, 2009; Xue et al., 2010) is given by the expression:

$$\omega(\boldsymbol{\sigma}_R) = 1 - \left( \frac{27J_3(\boldsymbol{\sigma}_R)}{2q_R^3} \right)^2 \quad (21)$$

where  $J_3(\boldsymbol{\sigma}_R) = \det(\boldsymbol{\sigma}'_R)$  is the third invariant of the stress deviator. For axisymmetric stress states  $\omega$  is equal to zero, while for all states consisting of pure or simple shear in addition to an arbitrary hydrostatic stress,  $\omega$  is equal to unity.

### 2.3. Numerical implementation of the constitutive models in FEM codes

#### 2.3.1. CDM model for fiber phase

The CDM model is implemented for finite element analysis using the user material interface (VUMAT) in the commercial code ABAQUS/Explicit (2005). The essential steps in the VUMAT update algorithm for the  $n$ th increment are described below.

1. Initialize the threshold strain at the beginning of the first increment as  $\varepsilon_D^{(0)} = \varepsilon_D^0$ .
2. Given  $\varepsilon_{ij}^{(n+1)}$ , evaluate the value of the equivalent strain  $\bar{\varepsilon}^{(n+1)} = \sqrt{2\varepsilon_{ij}^{(n+1)}\varepsilon_{ij}^{(n+1)}/3}$ .
3. If  $\bar{\varepsilon}^{(n+1)} < \varepsilon_D^{(n)}$  or  $\bar{\varepsilon}^{(n+1)} - \bar{\varepsilon}^{(n)} \leq 0$ , there is no additional damage. In this case, update the state variable with the unchanged values as  $\varepsilon_D^{(n+1)} = \varepsilon_D^{(n)}$ ,  $D^{(n+1)} = D^{(n)}$ . Proceed to step 5 with unchanged secant elastic stiffness  $E^{(n+1)} = E^{(n)}$  and unchanged secant stiffness tensor  $C^{(n+1)} = C^{(n)}$ .
4. If  $\bar{\varepsilon}^{(n+1)} \geq \varepsilon_D^{(n)}$  and  $\bar{\varepsilon}^{(n+1)} - \bar{\varepsilon}^{(n)} > 0$ , damage evolves. In this case:



- update the threshold as  $\bar{\varepsilon}_D^{(n+1)} = \bar{\varepsilon}^{(n+1)}$ ;
- update the damage state variable as  $D^{(n+1)} = D^{(n)} + \left(\frac{\bar{\varepsilon}^{(n+1)} - \bar{\varepsilon}^{(n)}}{2\varepsilon_0}\right)^{S^*} (\bar{\varepsilon}^{(n+1)} - \bar{\varepsilon}^{(n)})$ ;
- update the secant stiffness using Eq. (5) as  $E^{(n+1)} = (1 - D^{(n+1)})^2 E^0$ ;
- update the secant stiffness tensor using Eq. (4) as:

$$C_{ijkl}^{(n+1)} = \frac{E^{(n+1)}}{1 + \nu} \delta_{ik} \delta_{jl} + \frac{\nu E^{(n+1)}}{(1 + \nu)(1 - 2\nu)} \delta_{ij} \delta_{kl}$$

5. Update the stresses with the updated secant stiffness tensor  $C^{(n+1)}$  as  $\sigma_{ij}^{(n+1)} = C_{ijkl}^{(n+1)} \varepsilon_{ij}^{(n+1)}$ .

### 2.3.2. Strain-rate-dependent porous plasticity model for matrix phase

The finite deformation high-strain-rate-dependent porous plasticity constitutive relations are integrated by an extension of the backward Euler algorithm proposed by Aravas (1987) following the work in Paquet and Ghosh (2010). The rotated Cauchy stress is updated in the increment between the time steps  $t^{(n)}$  and  $t^{(n+1)}$  as

$$\sigma_R^{(n+1)} = \sigma_R^{(n)} + \Delta\sigma_R = \sigma_R^e - C^e : \Delta\varepsilon_R^p \quad (22)$$

where  $C^e$  is the fourth order isotropic elasticity tensor,  $\sigma_R^e = \sigma_R^{(n)} + C^e : \Delta\varepsilon_R$  is the elastic predictor for this integration algorithm, and  $\Delta\varepsilon_R^p = \Delta t (\mathbf{D}_R^p)^{(n+1)}$  is increment of rotated plastic strain tensor. Using an update algorithm, the rotated stress increment  $\Delta\sigma_R$  is calculated from a known increment in the strain tensor  $\Delta\varepsilon_R$ , which is related to the rotated strain increment  $\Delta\varepsilon_R$  as:

$$\Delta\varepsilon_R = (\mathbf{R}^T)^{(n+1)} \Delta\varepsilon \mathbf{R}^{(n+1)} \quad (23)$$

The stress increment is obtained by solving the nonlinear constitutive relations of Section 2.2.2 in the rotated Lagrangian coordinates.

Integrating Eq. (13) in the time step  $\Delta t$  between  $t^{(n)}$  and  $t^{(n+1)}$  by the backward Euler algorithm, the increment of rotated plastic strain  $\Delta\varepsilon_R^p$  can be decomposed into hydrostatic and deviatoric parts as

$$\Delta\varepsilon_R^p = \frac{1}{3} \Delta\varepsilon_{Rp} \mathbf{I} + \Delta\varepsilon_{Rq} \mathbf{n}_R^{(n+1)} \quad (24)$$

where  $\mathbf{n}_R = \frac{3}{2q_R} \sigma_R^e$  is a unit normal tensor representing the flow direction of the deviatoric plastic strain and  $\Delta\varepsilon_{Rp}$  and  $\Delta\varepsilon_{Rq}$  are the hydrostatic and deviatoric parts of  $\Delta\varepsilon_R^p$  respectively, expressed as:

$$\Delta\varepsilon_{Rp} = -\Delta\lambda \left(\frac{\partial\phi}{\partial p_R}\right)^{(n+1)}, \quad \Delta\varepsilon_{Rq} = \Delta\lambda \left(\frac{\partial\phi}{\partial q_R}\right)^{(n+1)} \quad (25)$$

Here  $p_R$  and  $q_R$  are hydrostatic and deviatoric components of the rotated Cauchy stress, given as:

$$\sigma_R = -p_R \mathbf{I} + q_R \mathbf{n}_R \quad (26)$$

Substituting Eq. (24) in Eq. (22) and expressing the elasticity tensor in terms of the shear and bulk moduli as  $C_{ijkl}^e = 2G\delta_{ik}\delta_{jl} + (K - \frac{2}{3}G)\delta_{ij}\delta_{kl}$ , the rotated Cauchy stress is expressed by the hydrostatic and deviatoric components of the incremental rotated plastic strain  $\Delta\varepsilon_{Rp}$  and  $\Delta\varepsilon_{Rq}$  as:

$$\sigma_R^{(n+1)} = \sigma_R^e - K\Delta\varepsilon_{Rp} \mathbf{I} - 2G\Delta\varepsilon_{Rq} \mathbf{n}_R^{(n+1)} \quad (27)$$

Eq. (27) implies  $\mathbf{n}_R^{(n+1)}$ ,  $(\sigma_R^e)'$  and the deviatoric part of  $\sigma_R^{(n+1)}$  are coaxial. So  $\mathbf{n}_R^{(n+1)}$  can be calculated from the elastic predictor  $\sigma_R^e$  as  $\mathbf{n}_R = \frac{3}{2q_R^e} (\sigma_R^e)'$ .

The resulting stress update algorithm is reduced to a two-parameter nonlinear problem involving the hydrostatic and deviatoric parts of the constitutive relations. The two nonlinear equations to be solved for  $\Delta\varepsilon_{Rp}$  and  $\Delta\varepsilon_{Rq}$  are derived from the flow rule and the viscoplastic law in the rotated Lagrangian frame, as enumerated below (Paquet and Ghosh, 2010).

- (1) *Rate-dependent flow rule:*  $\Delta\lambda$  can be eliminated from the two expressions in Eq. (25) and expressed in the rotated Lagrangian system as

$$\Delta\varepsilon_{Rp} \left(\frac{\partial\phi}{\partial p}\right)_R^{(n+1)} + \Delta\varepsilon_{Rq} \left(\frac{\partial\phi}{\partial p}\right)_R^{(n+1)} = 0 \quad (28)$$

where  $\Delta\varepsilon_{Rp}$  and  $\Delta\varepsilon_{Rq}$  are the hydrostatic and deviatoric parts of  $\Delta\varepsilon_R^p$  respectively. They satisfy the relations below.

- (2) *Viscoplastic law:* The first relation in Eq. (25) can be rewritten as

$$\Delta\varepsilon_{Rp} + \Delta\lambda \left(\frac{\partial\phi}{\partial p}\right)_R^{(n+1)} = 0 \quad (29)$$

Here the increment of viscoplastic multiplier, i.e.  $\Delta\lambda = \Delta t \dot{\lambda}^{(n+1)}$ , is derived from the integration of Eq. (15).

Eqs. (28) and (29) are iteratively solved for  $\Delta\epsilon_{Rp}$  and  $\Delta\epsilon_{Rq}$  using the Newton–Raphson method. Corrections  $c_p$  and  $c_q$  to the primary solution variables  $\Delta\epsilon_{Rp}$  and  $\Delta\epsilon_{Rq}$  are solved from the equations

$$A_{i1}c_p + A_{i2}c_q = b_i \quad i = 1, 2 \tag{30}$$

The coefficients  $A_{ij}$  and  $b_i$  are given in Appendix. The state variables  $\bar{e}_M^p, f$ , and  $\sigma_0$  are updated using the evolution equations below

$$\Delta\bar{e}_M^p = \frac{-p\Delta\epsilon_{Rp} + q\Delta\epsilon_{Rq}}{(1-f)\bar{\sigma}_M} \tag{31}$$

$$\Delta f = (1-f)\Delta\epsilon_{Rp} + A(\bar{e}_M^p)_R + k_\omega \omega f \Delta\epsilon_{Rq} \tag{32}$$

$$\Delta\sigma_0 = nB(\bar{e}_M^p)^{n-1} \Delta\bar{e}_M^p \tag{33}$$

Finally, the rotated plastic strain tensor  $(\epsilon_R^p)^{(n+1)}$  is obtained from Eq. (24) as:

$$(\epsilon_R^p)^{(n+1)} = (\epsilon_R^p)^{(n)} + \left( \frac{1}{3} \Delta\epsilon_{Rp} \mathbf{I} + \Delta\epsilon_{Rq} \mathbf{n}_R^{(n+1)} \right) \tag{34}$$

The stress  $\sigma^{(n+1)}$ , plastic strain  $(\epsilon^p)^{(n+1)}$  and corresponding increments are obtained by tensor rotation.

The constitutive law and accompanying integration scheme are implemented in the ABAQUS/Explicit (2005) finite element code via its VUMAT user material subroutine interface.

### 3. Simulation and results

#### 3.1. Material choice and parameters used

Aluminum matrix composites are widely used in aerospace structures, automobile components, semi-conductor packaging, impact mitigation and other engineering systems due to their high specific elastic modulus and specific strength (Lloyd, 1994; Clausen et al., 2004; Shalu et al., 2009; Brar et al., 2009; Hu et al., 2010). Aluminum 7075 alloys are candidate materials used in armor applications (Brar et al., 2009), and hence the alloy Al 7075-T6 is selected as matrix phase material for the simulations. On the other hand, silicon carbide (SiC) fibers, which have high specific strength and elastic modulus, excellent heat resistance and good high-temperature stability, are attractive for reinforcements in advanced lightweight composites. This is selected as the fiber material in these simulations. For SiC fiber reinforced Al 7075-T6 matrix composites, the material parameters for the isotropic CDM model of the SiC fiber, as well as for the GTN and Johnson–Cook constitutive models of the Al 7075-T6 matrix are given in Table 2. The properties for SiC (SCS-Ultra) are taken from Specialty Materials Inc. website (2010) and for Al 7075-T6 from Brar et al. (2009).

#### 3.2. Volume-averaged variables

The volume-averaged Cauchy stress and Lagrangian strain are given as (Nemat-Nasser, 1999)

$$\Sigma = \frac{1}{V} \int \sigma dV, \quad \mathbf{E} = \frac{1}{2} (\langle \mathbf{F} \rangle^T \langle \mathbf{F} \rangle - \mathbf{1}) \tag{35}$$

where  $V$  is the current total volume of the RVE,  $\langle \mathbf{F} \rangle = \frac{1}{V_0} \int \mathbf{F} dV_0$  is the volume-averaged measure of the deformation gradient  $\mathbf{F}$ , and  $V_0$  is the initial total volume of the RVE. In finite element analysis, the average stress and deformation gradient are rewritten as the weighted sum of the respective phase values as:

$$\Sigma = \frac{1}{V} \left( \sum_{k=1}^{N_f} \sigma_{f(k)}^e V_{f(k)}^e + \sum_{k=1}^{N_m} \sigma_{m(k)}^e V_{m(k)}^e \right), \quad \langle \mathbf{F} \rangle = \frac{1}{V_0} \left( \sum_{k=1}^{N_f} \mathbf{F}_{f(k)}^e V_{0f(k)}^e + \sum_{k=1}^{N_m} \mathbf{F}_{m(k)}^e V_{0m(k)}^e \right) \tag{36}$$

where  $N_f$  and  $N_m$  are the total number of elements in the fiber and matrix phases respectively,  $V_{f(k)}^e, V_{0f(k)}^e, \sigma_{f(k)}^e$  and  $\mathbf{F}_{f(k)}^e$  are the current and initial volumes, stress and deformation gradient in the  $k$ th element in the fiber phase, and  $V_{m(k)}^e, V_{0m(k)}^e, \sigma_{m(k)}^e$

**Table 2**  
Material constitutive parameters for the matrix and fiber.

Fiber	$E^0$ (GPa)	$\nu$	$\rho$ (kg/m <sup>3</sup> )	$\epsilon_D^0$	$\epsilon_0$	$S^*$			
	415	0.17	2800	0.0164	0.01	7.0			
Matrix	$E$ (GPa)	$\nu$	$\rho$ (kg/m <sup>3</sup> )	$f_N$	$s_N$	$\epsilon_N$	$f_0$	$f_C$	
	71.7	0.33	2810	0.01	0.1	0.3	0.0001	0.15	
	$f_F$	$f_u^*$	$A$ (MPa)	$B$ (MPa)	$C$	$n$	$m$	$k_\omega$	
	0.25	0.666667	546	678	0.024	0.71	1.56	1.0	

and  $\mathbf{F}_{m(k)}^e$  are the current and initial volumes, stress and deformation gradient in the  $k$ th matrix element. Energy absorption and dissipation are also important properties that relate to the localized deformation and damage in composites at high strain rates (Nemat-Nasser et al., 2007; Han et al., 1998). An estimate of the energy dissipation property is defined as the average non-recoverable energy density as:

$$W_D = \frac{1}{V} \left( \sum_{k=1}^{N_f} w_{Df(k)}^e V_{f(k)}^e + \sum_{k=1}^{N_m} w_{Dm(k)}^e V_{m(k)}^e \right) \quad (37)$$

where  $V_f = \sum_{k=1}^{N_f} V_{f(k)}^e$  and  $V_m = \sum_{k=1}^{N_m} V_{m(k)}^e$  are the current volumes of the fiber and the matrix respectively, and  $w_{Df}^e$  and  $w_{Dm}^e$  are the non-recoverable energy densities in elements of the fiber and matrix phases respectively. In the CDM model, the non-recoverable energy density in the  $k$ th fiber element ( $w_{f(k)}^e$ ) is defined as the dissipation energy density due to stiffness degradation (Carol et al., 1994)

$$w_{Df(k)}^e = -\frac{1}{2} \int \varepsilon_{ij(k)} \varepsilon_{ij(k)} dE_{(k)} \quad (38)$$

The non-recoverable energy density in the  $k$ th matrix element ( $w_{m(k)}^e$ ) is defined as the viscoplastic energy density:

$$w_{Dm(k)}^e = \int \sigma_{ij(k)} d\varepsilon_{ij(k)}^p \quad (39)$$

In a similar vein, an estimate of the absorption energy is assumed as the average recoverable energy density defined as

$$W_A = \frac{1}{V} \left( \sum_{k=1}^{N_f} w_{Af(k)}^e V_{f(k)}^e + \sum_{k=1}^{N_m} w_{Am(k)}^e V_{m(k)}^e \right) \quad (40)$$

where  $w_{Af}^e$  and  $w_{Am}^e$  are the recoverable energy densities in the fiber and matrix phase elements respectively. The recoverable energy density in the  $k$ th fiber element ( $w_{Af(k)}^e$ ) is given as:

$$w_{Af(k)}^e = \int \sigma_{ij(k)} d\varepsilon_{ij(k)} - w_{Df(k)}^e \quad (41)$$

whereas the recoverable energy density in the  $k$ th matrix element ( $w_{Am(k)}^e$ ) is defined as the elastic energy density:

$$w_{Am(k)}^e = \int \sigma_{ij(k)} d\varepsilon_{ij(k)} - w_{Dm(k)}^e = \int \sigma_{ij(k)} d\varepsilon_{ij(k)}^e \quad (42)$$

The total internal energy density  $W_T$ , corresponding to the sum of the absorption and dissipation energy densities is defined as

$$W_T = W_A + W_D = \frac{1}{V} \sum_{k=1}^{N_f} \int \sigma_{ij(k)} d\varepsilon_{ij(k)} V_{f(k)}^e + \sum_{k=1}^{N_m} \int \sigma_{ij(k)} d\varepsilon_{ij(k)} V_{m(k)}^e \quad (43)$$

The normalized energy absorption and energy dissipation are expressed as:

$$\widehat{W}_A = W_A/W_T, \quad \widehat{W}_D = W_D/W_T \quad (44)$$

### 3.3. Mesh convergence study

The problems are simulated using the trilinear 8-noded brick element with reduced integration (C3D8R) in ABAQUS. To evaluate the convergence characteristics of the finite element mesh for problems involving damage and failure, three meshes as shown in Fig. 5 are analyzed. The coarsest mesh in Fig. 5(a) is composed of 1512 elements in the fiber phase and 2576 elements in the matrix. The mesh in Fig. 5(b) consists of 3840 and 8000 elements in the fiber and matrix phases respectively, while the finest mesh in Fig. 5(c) is composed of 12,960 fiber elements and 25,560 matrix elements. A compressive load corresponding to a strain rate of  $10^5$  is applied to the RVE. The maximum time step for time integration is chosen as 0.01  $\mu$ s.

Damage in the fiber and the matrix is observed in all the three meshes at 3.5  $\mu$ s. Volume-averaged damage in the fiber is represented as:

$$\langle D \rangle = \frac{1}{V_f} \sum_{k=1}^{N_f} (D_{(k)}^e V_{f(k)}^e) \quad (45)$$

while volume-averaged damage in the matrix is given as

$$\langle f \rangle = \frac{1}{V_m} \sum_{k=1}^{N_m} (f_{(k)}^e V_{m(k)}^e) \quad (46)$$

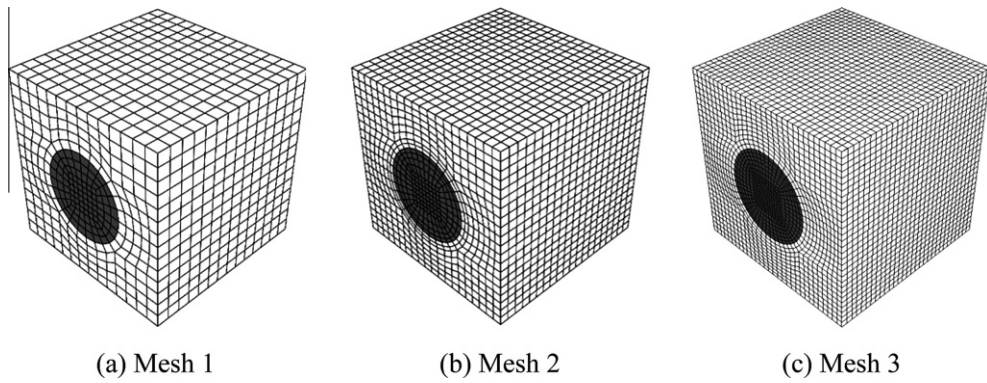


**Fig. 5.** Three different meshes used in a mesh convergence study: (a) coarsest mesh with 4088 elements; (b) intermediate mesh with 11,840 elements; and (c) finest mesh with 38,520 elements.

The convergence of these damage variables with mesh refinement is depicted in Fig. 6, demonstrating rapid convergence rates. An error estimate, based on the maximum difference in the effective strain as proposed in (Bass and Oden, 1987), is used to study mesh dependence. To evaluate the local error, the error estimate  $\Delta_m E_{local}$  over the  $m$ th incremental step is defined as

$$\Delta_m E_{local}^2 = \max_{k=1}^N (\Delta_m \bar{\epsilon}_{(k) \max}^2) \quad (47)$$

where  $\Delta_m \bar{\epsilon}_{(k) \max}$  is the maximum difference of the increment in effective strain between the  $k$ th element and its surrounding elements over the  $m$ th step. The local error  $\Delta_m E_{local}$  depends on the maximum value of the elemental error  $\Delta_m \bar{\epsilon}_{(k) \max}$ , evaluated over a total of  $N$  elements. To evaluate the overall error, the overall error estimate over the  $m$ th step  $\Delta_m E_{overall}$  is defined as

$$\Delta_m E_{overall}^2 = \frac{1}{V} \sum_{k=1}^N (\Delta_m \bar{\epsilon}_{(k) \max}^2 V_{(k)}^e) \quad (48)$$

where  $V_{(k)}^e$  is the volume of the  $k$ th element.

Table 3 gives an account of the local and overall error estimates. The error estimates are calculated at 1.5  $\mu$ s, which corresponds to progressive damage before failure, and at 4.0  $\mu$ s after failure has occurred. Generally the error reduces with increasing mesh density. Moreover, the error is less than  $10^{-3}$ , suggesting that the solution converges with increasing mesh

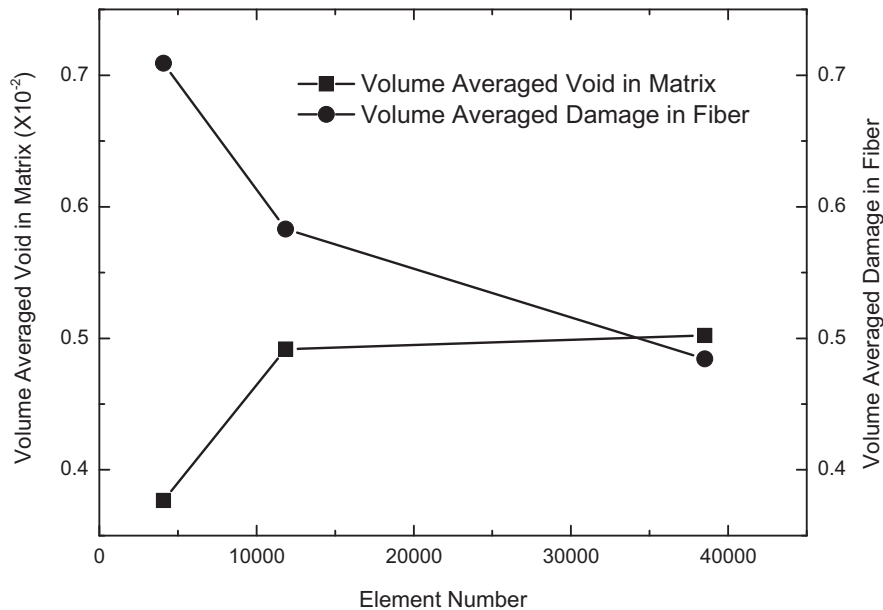


**Fig. 6.** Convergence in averaged damage variables with mesh refinement.

**Table 3**

Local and overall error estimates for different meshes.

Mesh no.	Time = 1.5 $\mu$ s		Time = 4.0 $\mu$ s	
	$\Delta E_{local}$	$\Delta E_{overall}$	$\Delta E_{local}$	$\Delta E_{overall}$
1	0.00075	0.00027	0.00018	0.00004
2	0.00057	0.00014	0.00018	0.00003
3	0.00038	0.00008	0.00018	0.00002

density and that all the three meshes are fine enough for this study. However, results in Table 3 also suggest that mesh sensitivity persists for problems involving damage. Usually, non-local theories such as gradient approaches (e.g. Fleck and Hutchinson, 1993; Hwang et al., 2002) are used for strain rate independent problems in order to incorporate size effects. These models have not been included in this study due to the presence of rate dependent matrix models. Subsequent simulations are constructed with the finest mesh 3.

### 3.4. Damage and failure mechanisms

Matrix damage is caused by the evolution of micro-voids that usually occur under the shear and tension dominated loading, while fiber damage is caused by high strains and corresponding stress concentrations. Therefore, under tensile or shear dominated loading, energy is dissipated in the matrix leading to localized deformation and damage evolution. Compressive loading leads to concentrated energy dissipation in the fiber leading to brittle fracture with very little matrix damage. Moreover, transient stress concentrations due to propagation and superposition of stress waves can be crucial for fiber failure. An example of damage and failure process at a strain rate of  $10^5 \text{ s}^{-1}$  is used to illustrate the two mechanisms below.

#### 3.4.1. Stress wave dominated damage and failure

In compression dominated loading, damage and failure usually are caused by stress waves, which experience multiple reflections, transmissions and interference in the presence of heterogeneities in the microstructure. Subsequently, these phenomena produce dynamic stress concentrations that are significantly greater than those in global average response (Pao and Mow, 1973) and may result in fiber damage and fracture. Fig. 7(a) depicts the normal stress ( $\sigma_{22}$ ) wave propagation along the loading direction  $X_2$  for the RVE with a unidirectional cylindrical fiber in Fig. 1(b). The size of the RVE is  $1 \times 1 \times 1 \text{ mm}^3$  and the cylindrical fiber volume fraction is 20%. The speed of the stress wave depends on the material properties. For elastic problems, the wave speed corresponds to the sonic speed  $c = \sqrt{E/\rho}$ , where  $E$  is Young's modulus and  $\rho$  is density. Using the initial (undamaged) modulus and density, the wave speeds in the matrix and the fiber can be roughly estimated to be 5.05 km/s and 12.17 km/s respectively. The initial properties can give a reasonable estimation of wave propagation since brittle failure is abrupt. Fig. 7(a) shows the stress wave propagation patterns predicted by the simulations, while Fig. 7(b) shows the normal stress ( $\sigma_{22}$ ) distribution along the loading direction at different simulation times. The main observations in Fig. 7(a) may be summarized as follows:

- (i) Under uniaxial loading, the stress waves from the two lateral loading surfaces travel into the matrix with a speed of 5.05 km/s, as shown by the line segments of  $A_1-B_1$  and  $A'_1-B'_1$ . At a time of 0.03  $\mu$ s, the peak of the stress wave should move about 0.15 mm from the boundary, which is shown clearly by the first curve in Fig. 7(b).
- (ii) When the stress waves reach the interface between the matrix and the fiber, a fraction of them are reflected e.g.  $B_1-A_2$  and  $B'_1-A'_2$ , while the other part is transmitted across the interface and goes into the fiber e.g.  $B_1-B'_2$  and  $B'_1-B_2$ . Since the fiber is stiffer than the matrix, the reflected stress wave has the same sign as the incident wave. This implies that a compression wave is reflected as a compression wave and an expansion wave as an expansion wave. On the interface, the superposition of the incident stress wave and the reflected stress wave causes stress concentration. The predicted time that the waves reach the interface is 0.05  $\mu$ s. From observing the stress distribution at 0.05  $\mu$ s in Fig. 7(b), the peak of the wave is found to be just on the interface and therefore the stress concentrates on the interface.
- (iii) In the fiber, the transmitted waves propagate as a higher speed of 12.17 km/s because of the higher modulus of the fiber. The waves meet in the middle of the fiber and the stress increases due to their superposition. Based on the wave speed, it is predicted that the waves meet in the fiber at about 0.07  $\mu$ s, which is also confirmed by the third graph in Fig. 7(b), which shows the sudden increase of the stress in the middle of the fiber.
- (iv) Subsequent to their superposition, the two waves part as seen in the fourth curve (0.09  $\mu$ s) of Fig. 7(b). When they reach the interface part of them is reflected and the other part is transmitted across the interface, which goes into the matrix. This is different from the first time when they reach the interface, because the matrix is much softer than the fiber. Here the compression wave is reflected as an expansion wave and the expansion wave is reflected as a compression wave. This effect is shown in the fifth curve (0.12  $\mu$ s) of Fig. 7(b), which shows a decrease of normal stress in the fiber.
- (v) In the matrix, the reflected waves propagate at a speed of 5.05 km/s towards the boundary of the RVE. When they reach the RVE boundary at points  $A_2$  and  $A'_2$ , they go through the boundary and into the matrix from the other side

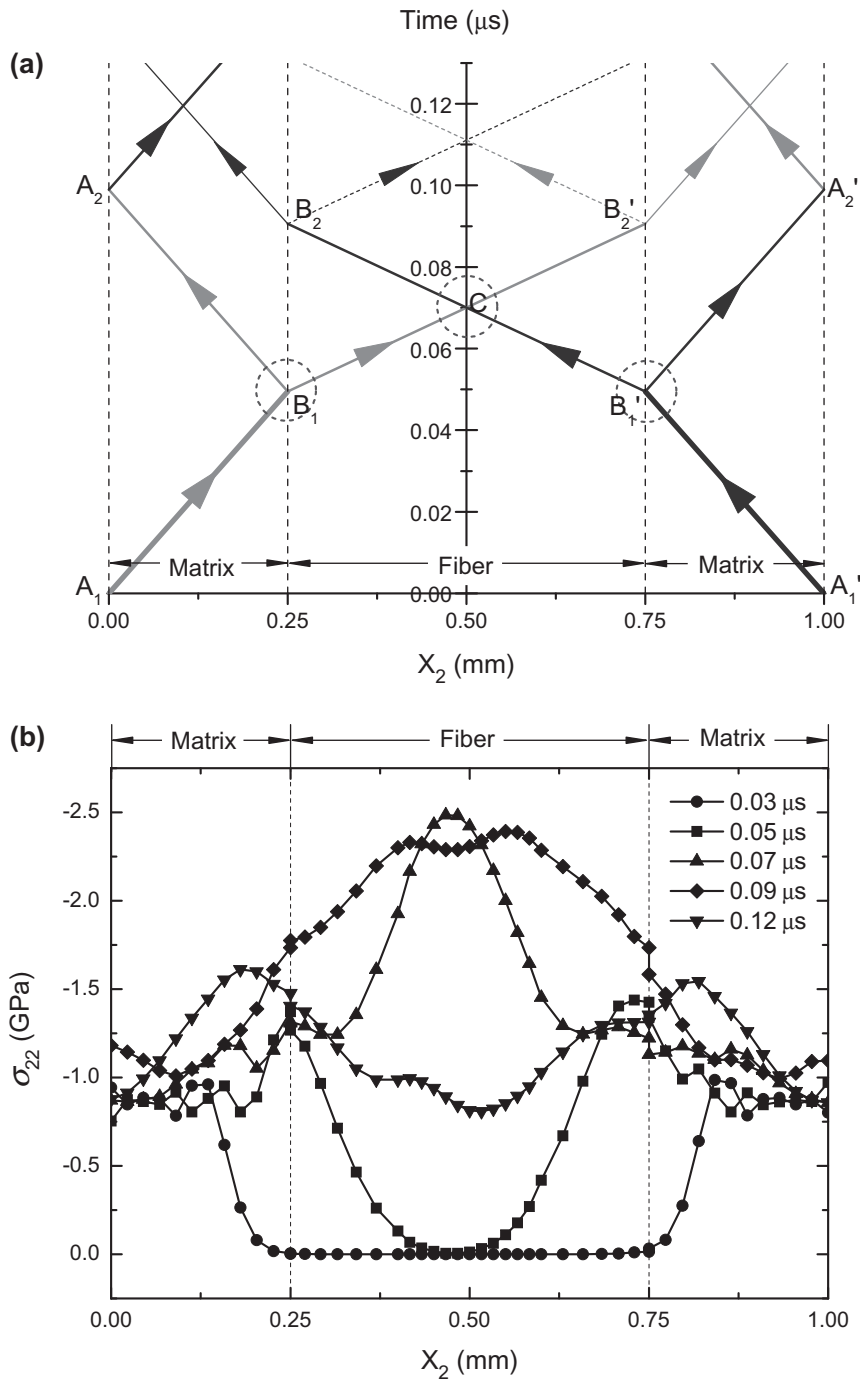


**Fig. 7.** Stress wave propagation in the RVE: (a) numerical prediction of time-position graph for wave propagation and (b) simulated result of stress distribution along the loading direction at different times.

due to periodic boundary conditions. Then along with the new loading-induced stress waves at that time, they propagate into the matrix and repeat the process analyzed above in a periodic manner. The time taken to traverse the distance from  $A_1$  to  $A_2$  (or from  $A_1'$  to  $A_2'$ ) is about  $0.099 \mu\text{s}$ .

From these observations of simulation results, it can be concluded that damage and failure may occur in the middle part of the fiber as well as at the interface, as marked by the dashed circles in Fig. 7(a). So the most probable time for failure in the

fiber is  $(0.099n + 0.070) \mu\text{s}$ , where  $n$  is a number count and  $0.070 \mu\text{s}$  is the time to travel from  $A_1$  (or  $A'_1$ ) to C. Similarly for failure on the boundary, the time is expected to be  $(0.099n + 0.049) \mu\text{s}$ , where  $0.049 \mu\text{s}$  is the time from  $A_1$  to  $B_1$  (or  $A'_1$  to  $B'_1$ ).

Fig. 8(a) depicts the damage and failure process in the RVE with a unidirectional cylindrical fiber under compressive loading. It indicates that fiber cracking in the middle of fiber is the predominant damage mode. Cracking begins at a time of  $3.34 \mu\text{s}$ , corresponding to a value  $n = 33$ . For another microstructure containing elliptical fibers, the period is calculated from the stress wave speed and the RVE geometry to be  $0.060 \mu\text{s}$ . Using the same analysis method of Fig. 7(a), the predicted time is obtained to  $(0.060n + 0.058) \mu\text{s}$  for fiber cracking, and  $(0.060n + 0.030) \mu\text{s}$  for interface failure. Numerical simulations in Fig. 8(b) shows the failure begins at the interface at a time of  $2.25 \mu\text{s}$ , corresponding to  $n = 37$ .

The phenomena of stress wave propagation, reflection, transmission and interference is also investigated for the transverse direction  $X_1$ , through the stress plots of Fig. 9(a). The response in this direction is much weaker than that along the loading direction  $X_2$ . Since no external load is applied in direction  $X_1$ , stress waves in this direction are not initiated at the boundary, but from the fiber–matrix interface, leading to their reflection and transmission. Along direction  $X_3$  however, no such phenomenon is observed as shown in Fig. 9(b), due to the lack of an interface in this direction. The stress in this direction does not change much with time. This is a consequence of periodicity conditions in this direction, implying an infinitely long fiber in this direction.

### 3.4.2. Void dominated damage and failure

Under tension and shear dominated loading, damage and failure are predominantly caused by the evolving microvoids in the matrix. Fig. 10 illustrates the evolution of the damage and failure phenomena in the RVE microstructure. In both cases, damage and failure occur in the matrix and the overall composite exhibits a ductile failure mode. Voids are initially diffused and not well defined and develop around interface due to stress concentration caused by the hard reinforcement. A portion of the matrix interface fails subsequently, reducing in the stresses in the failed portion. After initial debonding due to void growth, the matrix load cannot be effectively transferred into the fiber and hence the overall stress level in the fiber decreases. The remainder of the bonded matrix carries more stress, thereby extending debonding along the interface and finally leading to the failure of the entire interface. The damage distributions for the tensile and shear loads in Fig. 10(b) and (d) are similar, but with a  $45^\circ$  rotation, consistent with conventional mechanics theories. The tension and shear cases show similar damage evolution and failure modes although their deformed configurations are quite different. Debonding failure mode in tension has been experimentally investigated in Rao et al. (1993) for SiC-fiber reinforced 6061 aluminum alloy composites. Their experimental observation, shown in Fig. 10(e), has a similar overall damage profile as the numerical results in Fig. 10(d). Consistent with the experiments, the fiber phase in the simulations shows no evidence of fracture. Debonds are oriented along planes of maximum shear, about  $45^\circ$  to the principal stress plane.

The effect of inertia is much more pronounced for stress-wave dominated damage and failure in the fiber than for void dominated matrix damage and failure. Fig. 11 shows the normal stress ( $\sigma_{22}$ ) distribution along the loading direction  $X_2$  of the RVE (a) under quasi-static compressive load. Neither stress wave propagation nor stress wave superposition is observed in Fig. 11, which makes this significantly different from Fig. 7(b). The peak stress level is much lower than that with the inertia effect. At the beginning of the loading in the time range 0– $0.12 \mu\text{s}$ , the maximum  $\sigma_{22}$  is only about 1.0 GPa under quasi-static loading, in contrast to 2.5 GPa under dynamic loading. Consequently, the damage and failure processes are also different. Due to the lower stress level for quasi-static loading, failure occurs a little later than for dynamic loading. In the latter case, failure starts at  $3.34 \mu\text{s}$  at the center of the fiber and then expands into other parts of the fiber as shown in Fig. 8(a). On the other hand, the entire fiber fails simultaneously at  $3.36 \mu\text{s}$  in the former case. However, inertia effects present little influence on the void dominated damage and failure. For the cases of quasi-static shear and tensile loading, the failure mode and failure process are same as those for dynamic loading as shown in Fig. 10. At the beginning though, the stress distribution is similar to that for the compression case due to the absence of stress-wave propagation or superposition.

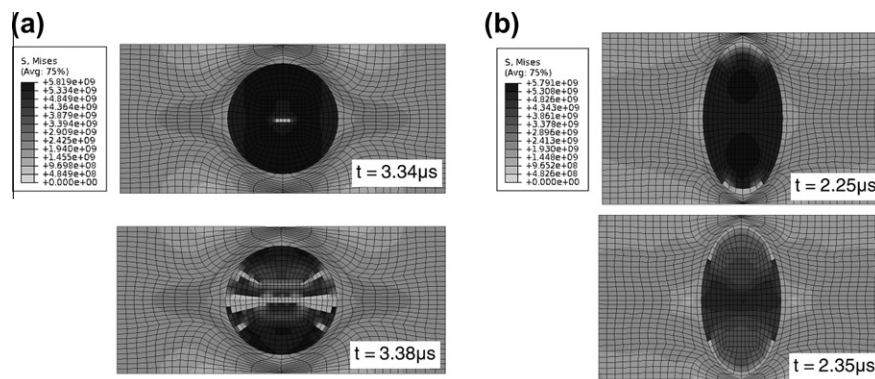


Fig. 8. Contour plots of the von Mises stress at different times: (a) cracking in the middle of the fiber and (b) failure at the fiber–matrix interface.

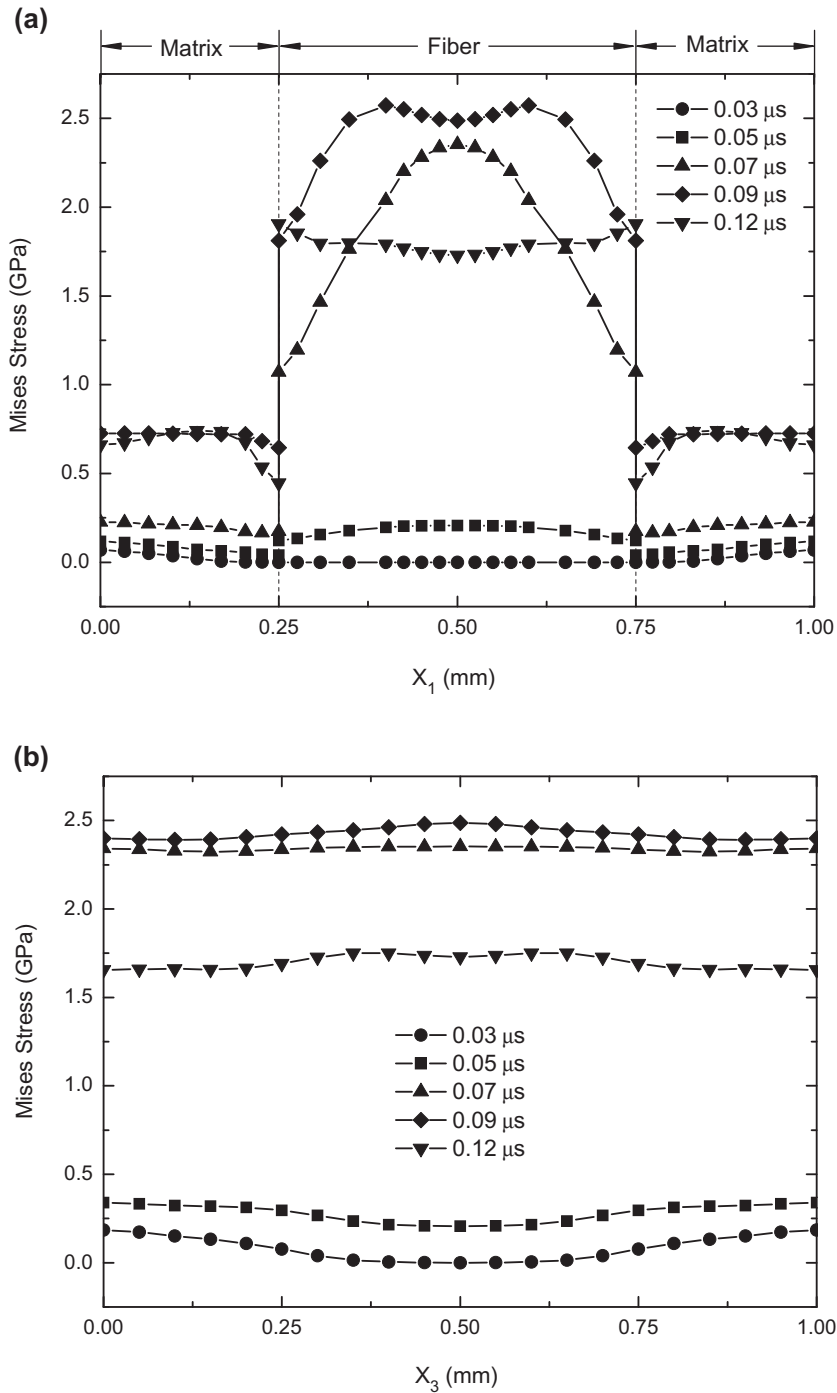
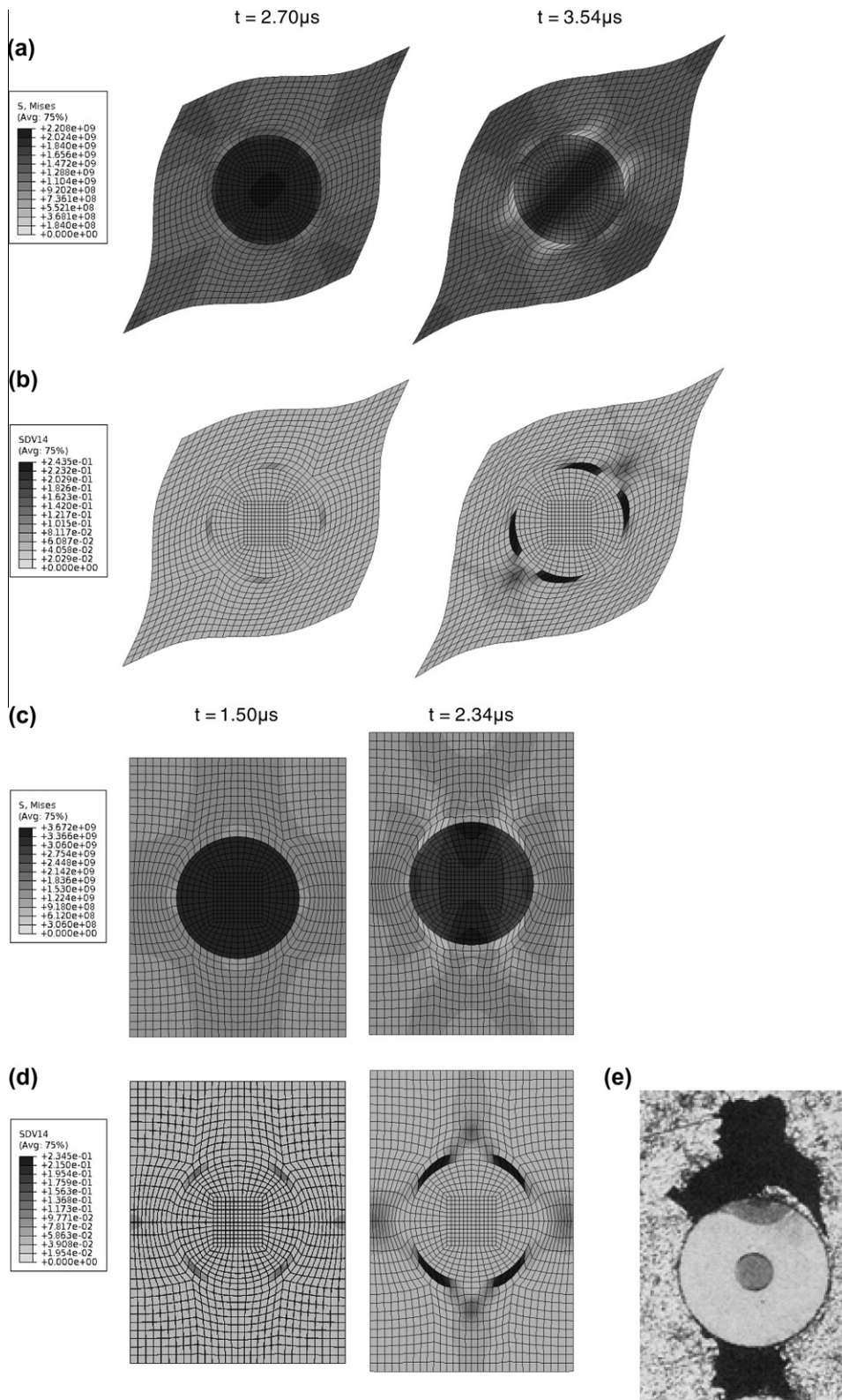


Fig. 9. von Mises stress distribution in the unit cell at different times: (a) along the transverse direction 1 and (b) along the fiber direction 3.

### 3.5. Factors influencing failure modes and energy absorption and dissipation

A number of factors influencing the damage and failure modes and the ability of energy absorption and dissipation of the metal-matrix composites are studied in this section. These include the effects of strain rate, loading type, fiber volume fraction and the microstructural morphology.





**Fig. 10.** Contour plots of von Mises Stress and void volume fraction at different times: (a) distribution of von Mises stress under shear loading; (b) distribution of void volume fraction (damage) under shear loading; (c) distribution of von Mises stress under tensile loading; (d) distribution of void volume fraction under tensile loading; and (e) experimental failure mode investigated in (Rao et al., 1993).

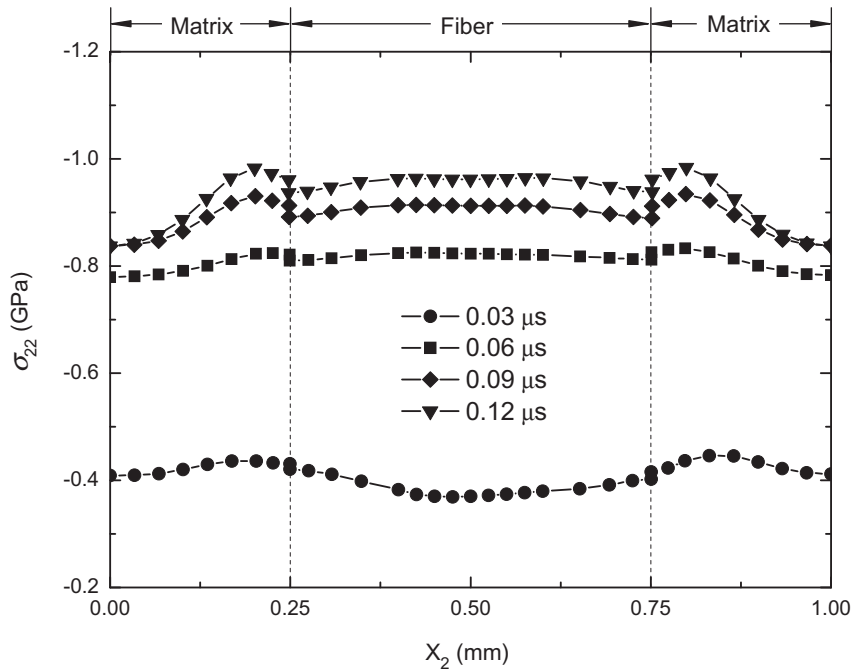


Fig. 11. Stress distribution along the loading direction  $X_2$  under quasi-static loading.

### 3.5.1. Effect of strain rate and loading type

Simulations are carried out for compression, tension and shear at strain rates ranging from  $10^3$  to  $10^5$   $s^{-1}$ , applied to the RVE in Fig. 1. The size of the RVE is  $1 \times 1 \times 1$   $mm^3$ . The plots of the average von Mises stress ( $\Sigma_{eq} = \sqrt{3\Sigma' : \Sigma'/2}$ ) as a function of the average strain component in the loading direction for the three types of loads are shown in Fig. 12(a)–(c) respectively. For comparison, results of corresponding rate-independent, quasi-static simulations are also plotted in these figures. Each curve depicts four stages of deformation and damage that the simulated microstructure undergoes. These include initial elastic deformation, plastic hardening followed by softening and post-softening behavior. The initial yield stress and the overall stresses increase with higher strain rates due to the rate dependent constitutive relations. The second stage witnesses the onset and evolution of void growth in the ductile matrix with plastic deformation. The maximum compressive stress in the compression loading is significantly higher than those for the tension and shear loading cases at all strain rates. Subsequently in the softening stage, different parts of the RVE fail in different modes depending on the type of loading. Significant stress differences between the rate-independent and rate-dependent cases cause early failure in the latter cases. Rise in stress for the dynamic problems is also enhanced by stress wave superposition, as demonstrated in Fig. 7. In the compression dominated loading of Fig. 12(a), the stress drops suddenly due to brittle fracture or crushing in the fiber with minimal ductile matrix damage. Larger stresses at higher strain rates cause early failure in the fiber. For shear and tension loaded cases, the stress decay is more gradual since the loss of stress carrying capacity is primarily caused by ductile failure due to growing voids in the matrix. While softening occurs much earlier in comparison with the rate-independent case, the onset strain of softening is less dependent on the strain rates due to the ductile nature of damage. Softening in tension occurs much earlier than that for the shear-loaded microstructure.

The post-softening stage also exhibits different behavior for the three loading cases. In Fig. 12(a), while the fiber has fragmented in compression, the matrix can still exhibit slight hardening with deformation. For the tension-dominated loading, the interface between the matrix and the fiber debonds, after which the fiber is not able to bear any tensile load. However it continues to resist compression from the transverse direction contact on both sides of the fiber as seen in Fig. 12(b). Softening due to void growth competes with limited hardening at this stage to cause staggered softening in the stress–strain curve at this stage. A similar behavior is also observed for the shear-dominated loading case in Fig. 12(c), though the extent of damage and loss in stress carrying capacity is much lower than that for the tensile case. In all cases, the presence of material rate dependence and inertia terms causes a much earlier failure than the rate-independent, quasi-static situations.

The dissipation energy in Eq. (37) is investigated for two special cases, viz. (i) no void in the matrix ( $f = 0$  and  $\dot{f} = 0$ ); and (ii) no fiber damage ( $D = 0$  and  $\dot{D} = 0$ ). While failure can only occur in the fiber in case (i), the matrix can still dissipate energy by plastic deformation corresponding to Eq. (37). This is evidenced by the energy dissipation plots under compressive and tensile loads in Fig. 13 with solid dots. The matrix energy dissipation continues to increase till fiber cracking causes a sharp increase in the fiber energy dissipation. For the tensile loading case, the failure strain is very large since matrix failure is inhibited. For the second case, damage in the fiber is restrained and hence there is no energy dissipated in the fiber as shown

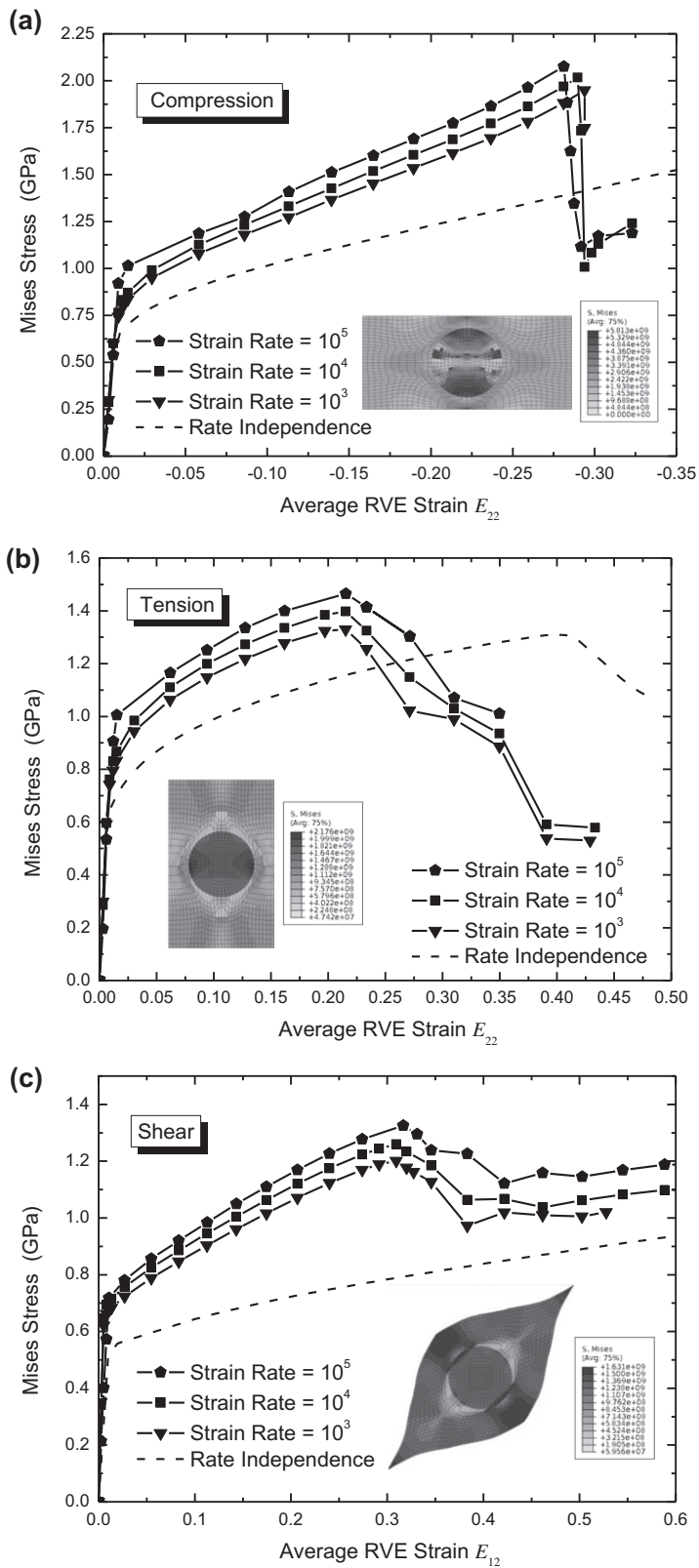
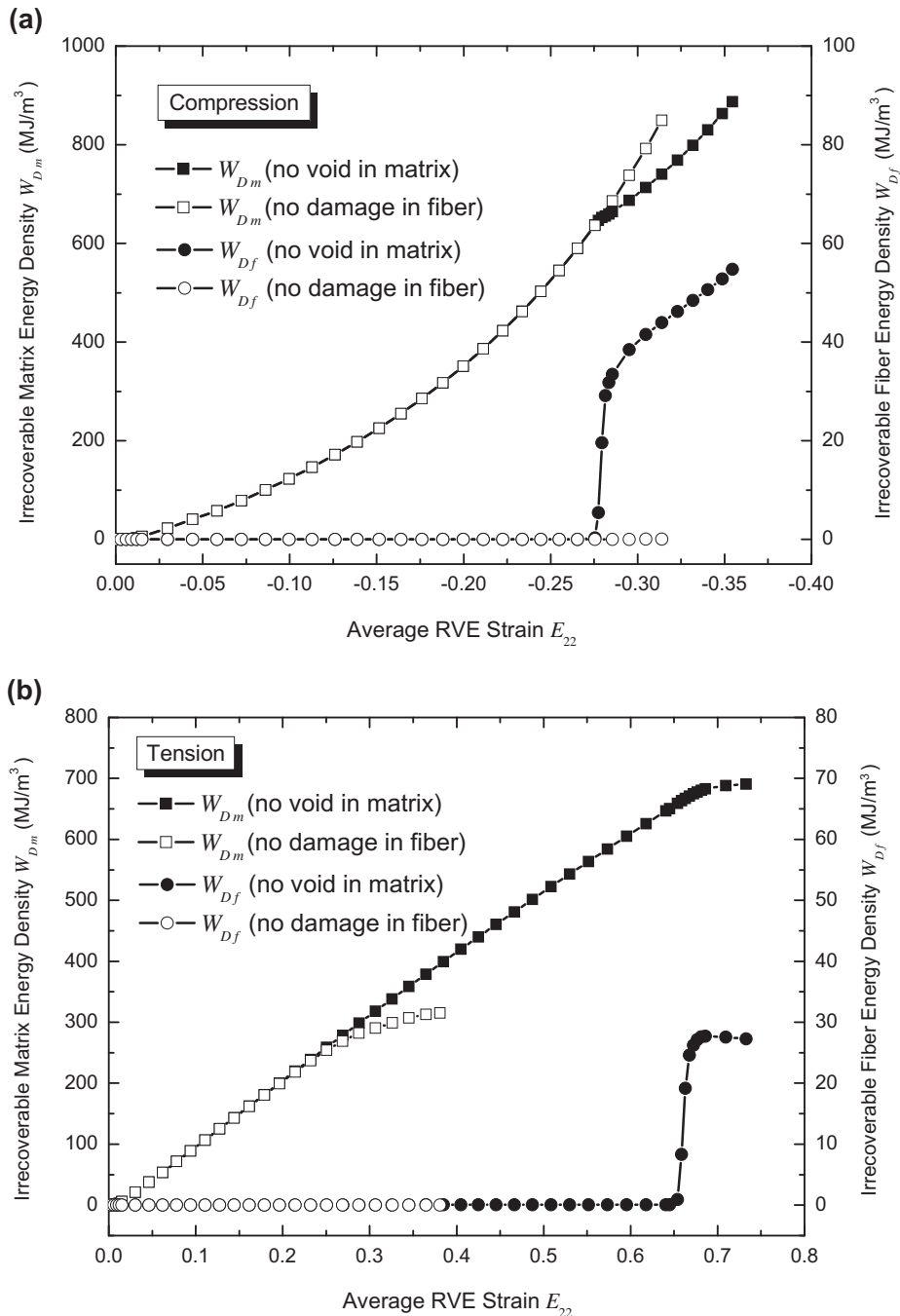


Fig. 12. Effect of strain rate under different loading conditions: stress–strain plots under (a) compression; (b) tension; and (c) shear loading.



**Fig. 13.** Energy dissipation plots as a function of macroscopic strain for two special cases corresponding to only fiber damage and only matrix under (a) compressive loading and (b) tensile loading.

by the plot with hollow dots in Fig. 13. The matrix energy dissipation, on the other hand, continuously increases until final matrix rupture.

Fig. 14 depicts the evolution of absorption and dissipation energy in Eqs. (40) and (37), as well as the damage evolution in the fiber and matrix phases of the RVE loaded in compression at a strain rate of  $10^4 \text{ s}^{-1}$ . In order to show the damage evolution quantitatively, the damaged fiber volume fraction  $\hat{V}_{fD}$  and damaged matrix volume fraction  $\hat{V}_{mD}$  are expressed respectively as

$$\hat{V}_{fD} = V_{fD}/V_f, \quad \hat{V}_{mD} = V_{mD}/V_f \quad (49)$$

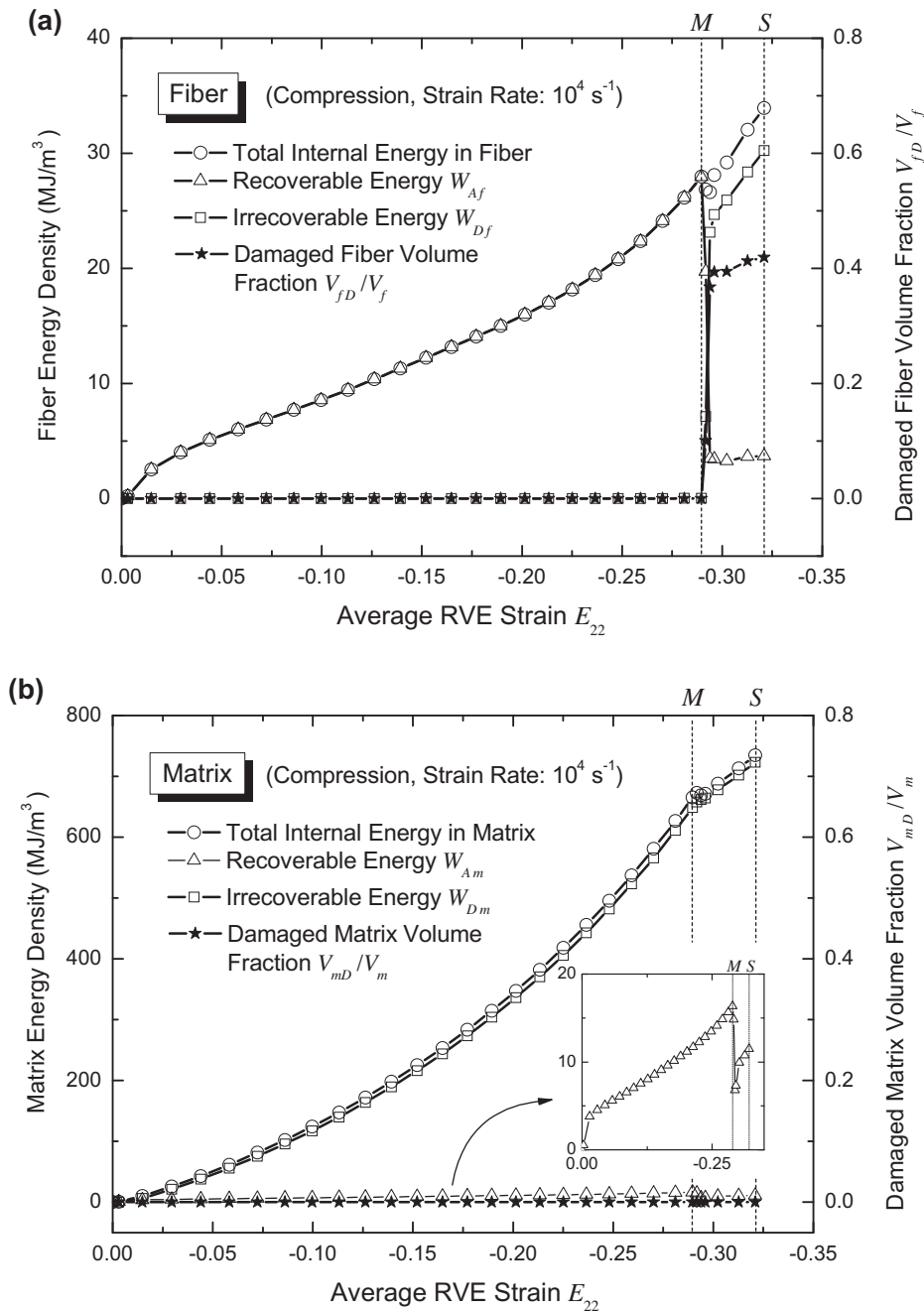


Fig. 14. Energy and damage evolution under compressive load: (a) in the fiber and (b) in the matrix.

where  $V_{fD}$  and  $V_{mD}$  are the damaged volumes of the fiber and the matrix respectively. An element is assumed to be damaged when its average damage level reaches a critical value. The damaged fiber volume  $V_{fD}$  is assumed to be

$$V_{fD} = \sum_{k=1}^{N_f} H[D_{(k)}^e - 0.8] V_{f(k)}^e \quad (50)$$

where  $D_{(k)}^e$  represents the damage in the  $k$ th element in the fiber, and 0.8 corresponds to a threshold value based on the observation that rapid failure occurs once an element has damaged more than 80%. Similarly, the damaged matrix volume  $V_{mD}$  is defined as

$$V_{mD} = \sum_{k=1}^{N_m} H[f_{(k)}^e - f_c] V_{m(k)}^e \quad (51)$$

where  $f_{(k)}^e$  is the void volume fraction in the  $k$ th element. When  $f_{(k)}^e$  reaches the critical value  $f_c$  in Eq. (9), void growth is accelerated and the void volume fraction reaches its failure value  $f_f$  in a very short time.

The fiber responses are shown in the graphs of Fig. 14(a). Before fiber damage, there is no energy dissipation in the fiber and all the energy is absorbed. When the macroscopic Lagrangian strain reaches a value of approximately 0.29, the damaged fiber volume fraction  $\hat{V}_{fD}$  climbs sharply, which suggests fiber brittle fracture. At this time, the energy absorption drops suddenly, while most of the energy is dissipated by fiber fracture. This sudden drop occurs at the point  $M$  in the graph for which the value of absorbed energy is a maximum. Beyond this point, the damaged fiber volume fraction  $\hat{V}_{fD}$  saturates with the absorption energy remaining at a very low value, and the dissipation energy increasing after a sharp ascent. The damaged fiber volume fraction  $\hat{V}_{fD}$  saturates at the point  $S$  in the graph of Fig. 14. The fiber damage also affects the matrix behavior as shown in Fig. 14(b). Although there is no matrix failure ( $\hat{V}_{mD} \equiv 0$ ), there is a sudden change in the matrix energy. The matrix absorbs and dissipates viscoplastic energy at the same time before fiber cracking. At the point  $M$ , the average stress level in the matrix decreases due to the fiber fracture, causing a sudden release in the absorption energy with a slower energy dissipation.

At point  $M$ , the volume-averaged von Mises stress and energy absorption reach their maximum values  $\Sigma_{eq}^M$  and  $W_A^M$  respectively. At point  $S$ , the damaged fiber volume fraction  $\hat{V}_{fD}$  reaches its saturation value  $\hat{V}_{fD}^S$  and the energy dissipation is noted as  $W_D^S$ . The effects of strain rate on the volume fraction  $\hat{V}_{fD}^S$ , the energy absorption  $\hat{W}_A^M = W_A^M/W_T$  and the energy dissipation  $\hat{W}_D^S = W_D^S/W_T$  are all shown in Fig. 15. At a higher strain rate, the energy cannot be dissipated as effectively as at the lower strain rate. Consequently, the material absorbs a larger percentage of energy, which results in higher stresses and damage. Thus with increasing strain rate, the maximum volume-averaged von Mises stress  $\Sigma_{eq}^M$ , the saturation value of damaged fiber volume fraction  $\hat{V}_{fD}^S$ , and the percentage of energy absorption all increase, and the percentage of energy dissipation decreases.

Results for the tension-loaded case are shown in Figs. 16–18. In this case, there is no damage in the fiber, as shown in Fig. 16(a). Instead, ductile damage occurs in matrix, as shown in Fig. 16(b). Distinct from the sudden change due to brittle fracture in the compression loading case, damage increases gradually, while the energy absorption decreases gradually for tensile loading. The staggered increase in matrix damage  $\hat{V}_{mD}$  corresponds to the four stages of softening in stress–strain response, viz. damage initiation, damage growth, damage coalescence and damage expansion across the RVE. This is shown in the four damage contours of Fig. 17. When the damaged portions coalesce and transcend the RVE, neither the energy dis-

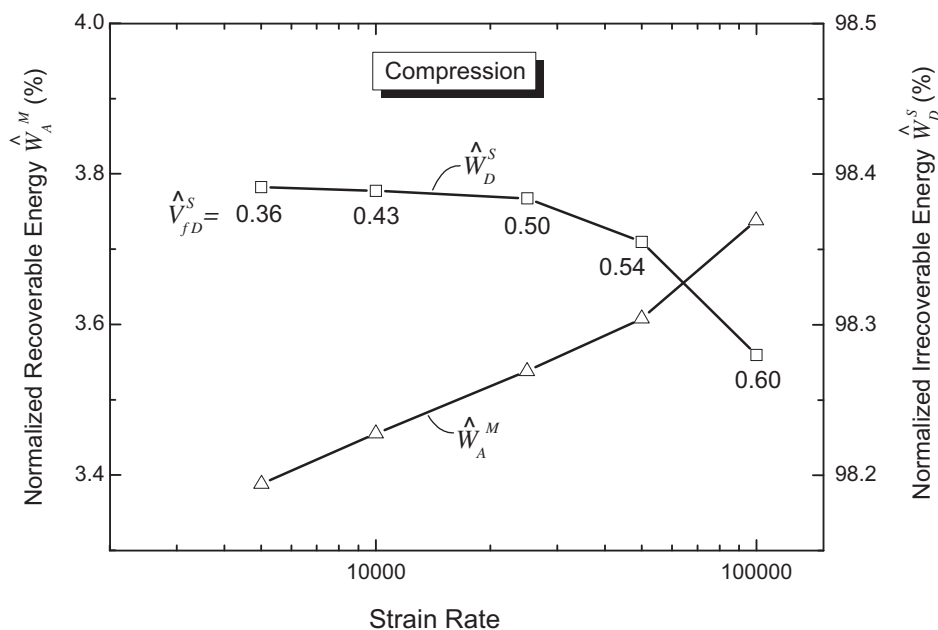


Fig. 15. Strain rate effect on the energy absorption and dissipation under compressive load.

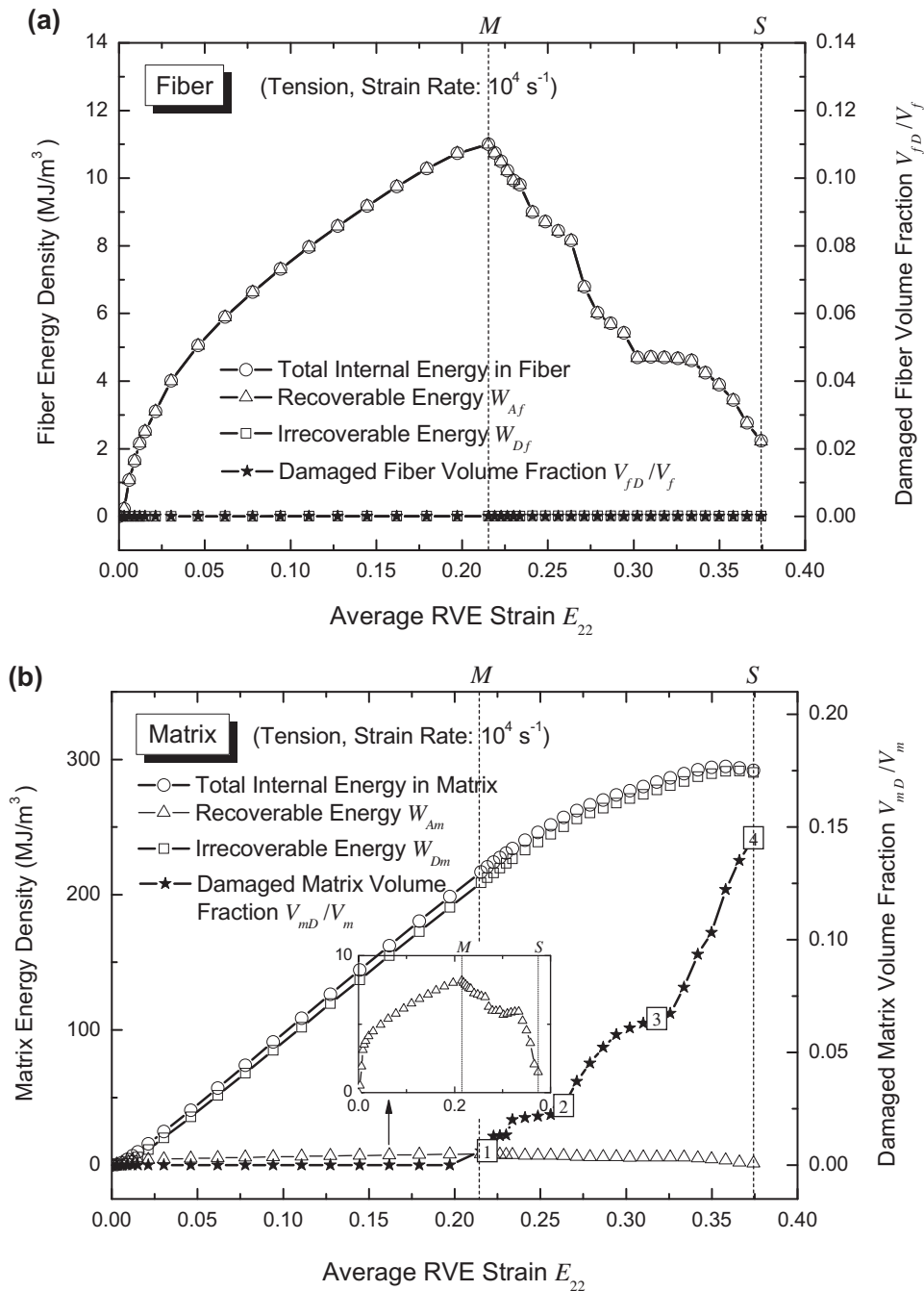


Fig. 16. Energy and damage evolution under tensile load: (a) in the fiber and (b) in the matrix.

sipation nor the damaged matrix volume fraction can increase any further corresponding to point S in Fig. 16. The point M represents the onset of damage.

For the tension loaded case, the effects of strain rate on  $\widehat{V}_{mD}^S$ ,  $\widehat{W}_A^M$  and  $\widehat{W}_D^S$  are depicted in Fig. 18. Similar to the compression loaded case, the energy at higher strain rates cannot be dissipated effectively and the material absorbs a higher percentage of energy. However, in contrast to the compression case, the damaged matrix volume fraction remains around 13–15%, and slightly decreases with an increase in strain rate. Failure in the compression loaded case is dominated by the stress wave phenomenon with severe superposition and reflection effects at higher strain rates, whereas failure in the tension loaded case is dominated by void evolution reaching above a critical value. As suggested in Fig. 18, this critical value of void volume fraction is almost a constant and decreases only slightly with increasing strain rates.

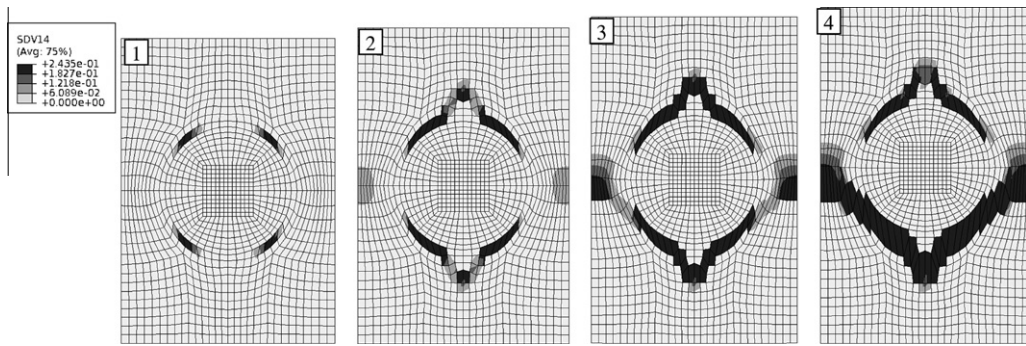


Fig. 17. Contour plots of damage evolution under tensile load at strain rate of  $10^4 \text{ s}^{-1}$ .

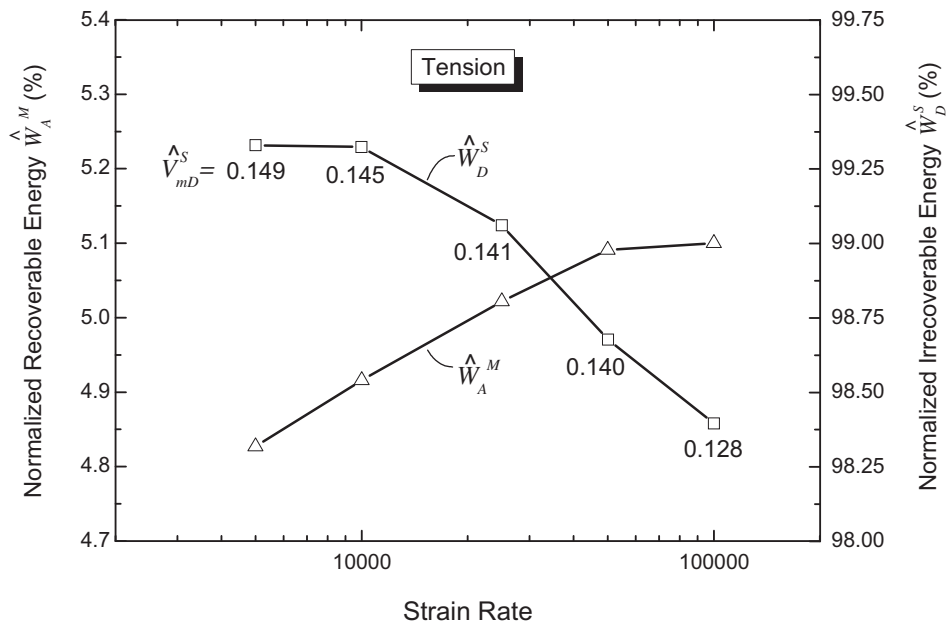


Fig. 18. Strain rate effect on the energy absorption and dissipation under tensile load.

### 3.5.2. Effect of volume fraction

The square-array unidirectional, cylindrical fiber reinforced composite RVE in Fig. 1 is again investigated to study the effect of volume fraction on failure mode and energy absorption. The studies are conducted at a strain rate of  $10^5 \text{ s}^{-1}$ . The fiber volume fraction is varied from 7% to 38%. The effect of fiber volume fraction is shown in Figs. 19 and 20 respectively. The failure modes for different fiber volume fractions are presented through von Mises stress contours in the deformed RVE that is extracted from the most damaged region. Fig. 19(a) shows the recoverable or absorption energy for the compression and tension loaded cases. At lower fiber volume fractions, the absorbed energy increases with the increasing volume fraction. For the compression loaded case, the energy absorption reaches a higher level and saturates gradually. Higher fiber volume fraction leads to higher overall stress in the fiber, which raises the energy absorption. However, larger volume fractions (in excess of 30%) of the hard fiber can restrain RVE deformation, decreasing the overall strain and the energy absorption slightly. For the tension loaded case, the energy absorption characteristics are slightly different as shown with the dashed curve in Fig. 19(a) that saturates quickly. At higher volume fractions (above 13%), it decreases and stays at a lower level due to loss of stress carrying capacity with early interfacial debonding.

Fig. 19(b) shows the energy dissipation characteristics for the compression and tension loaded cases. For both cases, the dissipation energy increases at lower volume fractions, reaches a peak at a threshold value and subsequently decreases. The dissipation energy dependence on volume fraction follows a transition between different failure modes in the RVE. For lower fiber volume fractions under compressive loading, failure initiates at the center of the fiber with cracks parallel to the loading direction, due to requirements of transverse elongation imposed by the ductile matrix surrounding the brittle SiC fiber. As shown in Fig. 20(a), this failure mode is investigated in RVE simulations with 7%, 10% and 13% fiber volume fraction. The



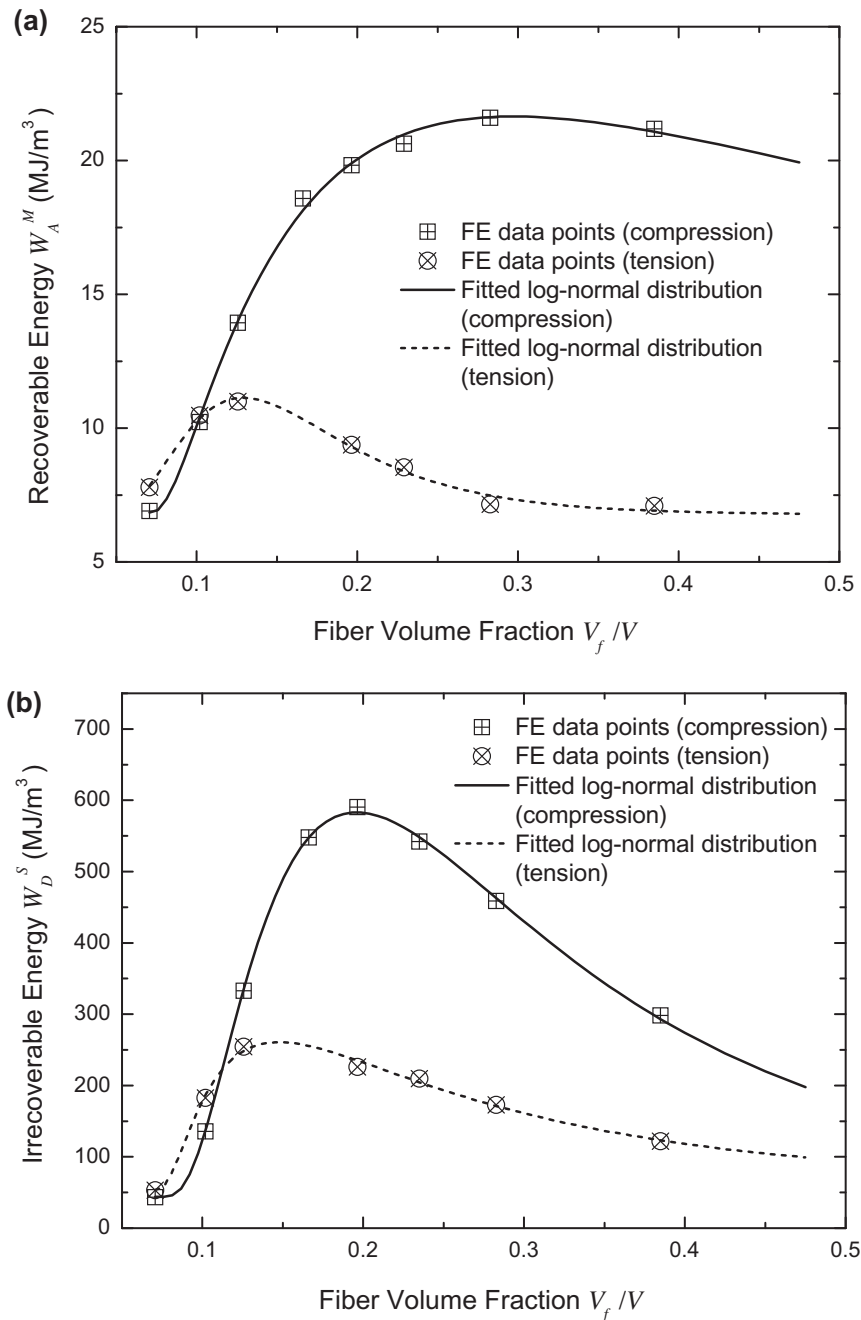


**Fig. 19.** Energy absorption and dissipation of RVEs with different volume fractions under compression and tension loading at a strain rate of  $10^5 \text{ s}^{-1}$ : (a) energy absorption and (b) energy dissipation.

crack direction changes with increasing fiber volume fraction as shown in Fig. 20(b), where e.g. with 17% and 20% volume fractions the fiber begins to crack in both directions. This signals a transition regime. RVE's with higher volume fractions, e.g. 23%, 28% and 38%, the fiber begins to crack vertically along the loading direction as shown in Fig. 20(c). With increasing fiber volume fraction and decrease in matrix proportion, the effect the transverse elongation becomes less important and instead the effect of longitudinal compression takes a more important role. In the two transition regime ( $\sim 17\text{--}20\%$ ), the effects of the transverse elongation and longitudinal compression are similar. In the cases of higher fiber volume fraction (23%, 28% and 38%), longitudinal compression completely dominates the failure mode. Energy dissipation saturates in the transition region of the failure mode, implying that fiber volume fractions for which effects of both transverse elongation and longitudinal compression are strong correspond to the highest energy dissipation. Similarly under tensile loading, failure modes transition in the saturation region of energy dissipation. For lower fiber volume fraction, transverse contraction of the ductile

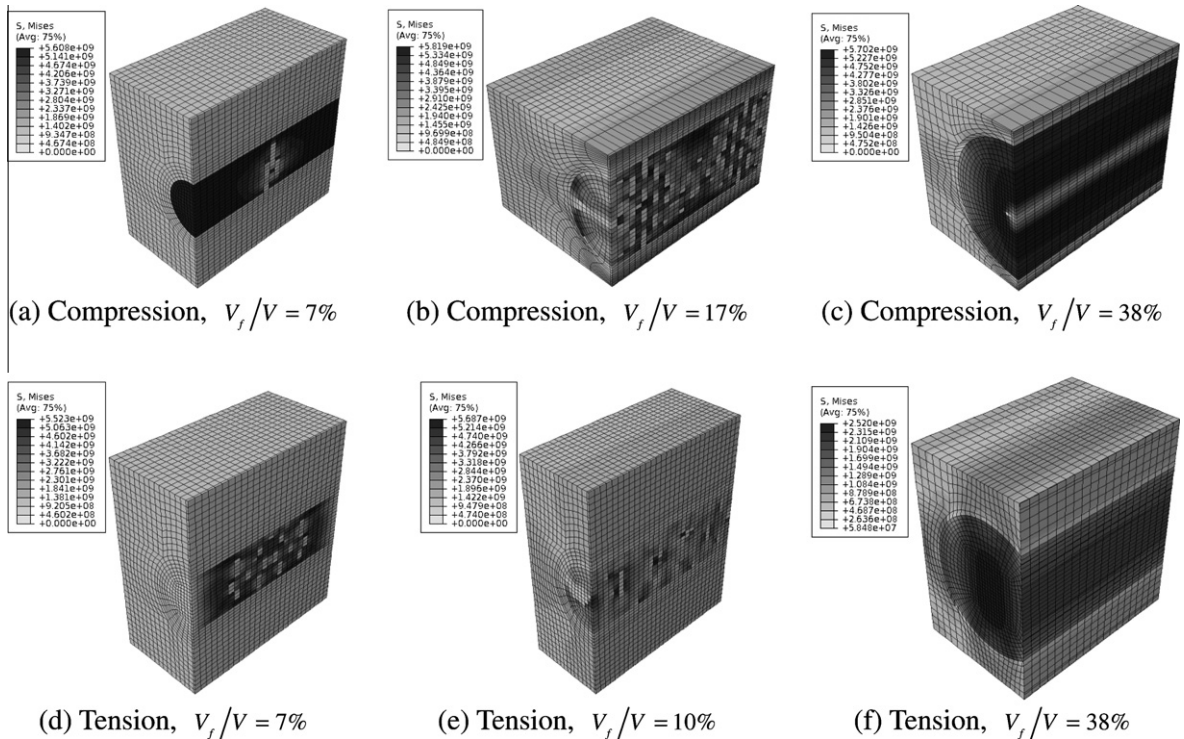


**Fig. 20.** Failure modes of RVEs with different volume fractions under compression and tension at a strain rate of  $10^5 \text{ s}^{-1}$ : (a)–(c) failure modes under compression for different fiber volume fractions; (d)–(f) failure modes under tension for different fiber volume fractions.

matrix causes crushing of the brittle SiC fiber as shown in Fig. 20(d) for 7% fiber volume fraction. With the increasing of fiber volume fraction, longitudinal tension dominates and the failure mode transitions to interfacial debonding. Fig. 20(e) shows this transition for 10% fiber volume fraction, with both fiber cracking and interfacial debonding modes. For the RVE with 38% fiber volume fraction in Fig. 20(f), the failure mode has changed to interfacial debonding.

For SiC fiber reinforced Al 7075-T6 composites, the simulation results conclude that neither low nor high fiber volume fraction can improve the ability of energy absorption and dissipation effectively. The optimal fiber volume fraction for energy absorption and dissipation is around 20% for compression dominated cases and 15% for tension dominated cases.

### 3.5.3. Effect of microstructure

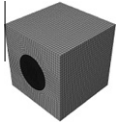
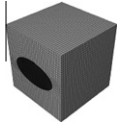
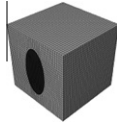
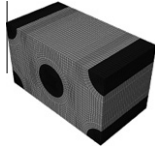


Six different periodic microstructures, shown in Table 4, are simulated to investigate failure modes as well as their energy absorption and dissipation characteristics. The volume is  $1 \text{ mm}^3$  for the RVEs (a)–(c), and  $2 \text{ mm}^3$  for the RVEs (d)–(f). The simulation strain rate is  $10^5 \text{ s}^{-1}$  and the fiber volume fraction of all the six microstructures is 20%. The failure modes and energy absorption and dissipation statistics for the different microstructures are tabulated in Table 4.

From RVE's (b), (a) and (c), the effect of the aspect ratio of the fiber, defined as the ratio of the fiber axial length in direction  $X_1$  to that along the loading direction  $X_2$ , can be observed. The aspect ratios of the fiber in RVEs (b), (a) and (c) are 2.0, 1.0 and 0.5, respectively. Neither high nor low aspect ratio is good for energy absorption or dissipation under compressive loading, as shown in Table 4. The fiber with moderate aspect ratio, RVE (a), has the best ability to absorb and dissipate energy among the three RVEs. In RVE's (b) and (c), the higher curvatures at the poles of the ellipse can easily cause stress concentration, leading to debonding failure. Under tensile loading, RVE (a) also has the best ability to absorb energy, but RVE (c), with the lowest fiber aspect ratio, dissipates the most energy among the three RVEs. In this case, the failure modes for all the three RVEs are void dominated matrix debonding. Consequently the stress concentration due to high curvature can only affect the initiation of the damage, which only has some influence on the energy absorption. The softening process from point M to point S is dominated by the void evolution. RVE (c) can endure a longer softening process and reach higher failure strain. Thus it has better ability of energy dissipation.

Investigating RVEs (a)–(f) in Table 4, the following major observations are made from these characteristics.

- (1) Under compressive loading, the levels of energy absorption are similar for all microstructures varying from  $14.53$  to  $25.25 \text{ MJ/m}^3$ . This result corroborates the fact that energy absorption predominantly depends on the fiber volume fraction for compression loaded microstructures. Microstructures with unidirectional fibers (RVEs (a)–(e)) have better energy absorption characteristics than that for the cross-ply fibers (RVE (f)), with the highest for the hexagonal arrangements.

**Table 4**Comparison of energy absorption  $W_A^M$ , dissipation  $W_D^S$  and failure mode characteristics among different microstructures (the compressive and tensile loads are applied on the top and bottom surfaces of the RVE).

Microstructure		(a) RVE with a cylindrical fiber	(b) RVE with an elliptical fiber	(c) RVE with an elliptical fiber	(d) Rectangular RVE with hexagonal arrangement of fibers	(e) Rectangular RVE with hexagonal arrangement of fibers	(f) Cross-ply RVE with orthogonal fibers
							
Compressive load	$W_A^M$ (MJ/m <sup>3</sup> )	19.82	18.91	15.23	20.40	25.25	14.53
	$W_D^S$ (MJ/m <sup>3</sup> )	590.23	494.28	322.245	600.85	996.97	27.87
	Failure mode	Fiber cracking	Matrix debonding	Fiber debonding	Fiber cracking	Fiber cracking	Fiber failure
Tensile load	$W_A^M$ (MJ/m <sup>3</sup> )	9.37	9.17	8.04	9.87	9.19	14.19
	$W_D^S$ (MJ/m <sup>3</sup> )	239.55	212.55	246.53	414.81	242.08	93.8214
	Failure mode	Matrix debonding	Matrix debonding	Matrix debonding	Matrix failure	Matrix debonding	Fiber failure

- (2) Energy dissipation characteristics under compressive loading have a strong dependence on the microstructure. The unidirectional cylindrical fiber-based RVEs (a), (d) and (e) have high energy dissipation values, with RVE (e) being the highest (~60% higher than the others). The corresponding failure mode is fiber cracking. RVEs (b) and (c) with unidirectional elliptical fibers undergo moderate energy dissipation with interfacial debonding failure at locations of highest curvature (poles of the ellipse). In RVE (b), transverse elongation dominates and the interfacial debonding initiates in the matrix, while in RVE (c) longitudinal compression dominates, and debonding initiates in the fiber. The RVE (b) has higher energy absorption properties than RVE (c), while the cross-ply fiber microstructure (RVE (f)) has a low energy dissipation characteristic. In the latter case, the transverse deformation in both directions is constrained by the hard and brittle SiC fibers and even a small deformation can cause fiber failure.
- (3) Under tensile loading, RVEs (a)–(e) with unidirectional fibers have similar energy absorption characteristics, varying from 8.04 to 9.87 MJ/m<sup>3</sup>. The RVE (f) however has about 50% higher absorption capability, since both the transverse directions are constrained by the hard fiber.
- (4) RVEs (a)–(e) with unidirectional fibers have high ductility and possess good energy dissipation properties under tensile loading, with RVE (d) being the highest. The primary failure mode for all the RVEs is interfacial debonding. Similar to item (2), the RVE (f) with cross-ply fibers has the lowest energy dissipation under tensile loading.

In view of the energy absorption and dissipation properties, microstructures (d) and (e) with hexagonal arrangement of fibers are desirable. In addition, RVE (e) possesses the highest compressive energy dissipation property in one direction, while RVE (d) has the highest tension energy dissipation ability in another direction. It should be noted that microstructures with hexagonal arrangement of fibers RVEs (d) and (e) are nearly isotropic for elastic behavior. However, their plastic and damage behavior induces significant anisotropy with increasing deformation.

#### 4. Conclusions

This paper investigates the effect of microstructural morphology and loading characteristics on micromechanical stress-wave propagation leading to different damage mechanisms, energy absorption and dissipation characteristics. The material microstructure is represented by a brittle fiber in a ductile matrix in different arrangements. The matrix material behavior is modeled using a high-strain-rate dependent elastic-viscoplastic constitutive model with damage evolution. This model is based on the extended GTN model with a Johnson–Cook type hardening law. It accounts for damage evolution, strain-rate dependence and shear-dominated failure in the matrix. Damage in the fiber is modeled by an isotropic continuum damage mechanics (CDM) model. The damage and failure mechanisms are studied to comprehend microstructural deformation and damage mechanisms at high strain rates ( $10^3$ – $10^5$  s<sup>-1</sup>). Two types of damage and failure mechanisms are investigated in this paper, viz. stress wave dominated and void dominated damage and failure. The former mechanism prevails in compression dominated loading, in which the transmission, reflection and interference of stress waves play an important role in fiber cracking at the center or interfaces. The latter mechanism dominates in shear and tension loading, for which damage is governed by void nucleation, growth and coalescence in the matrix. For both mechanisms, stress wave propagation makes the materials under high strain-rate loading fail at much lower strain levels than those under quasi-static and low strain-rate loadings.

The influence of strain rate, loading type, fiber volume fraction and microstructure on the failure modes, as well as on energy absorption and dissipation properties, are investigated for SiC fiber/Al7075-T6 composites under high strain-rate loading. Three different failure modes are investigated, viz. fiber cracking, debonding initiating in the matrix and debonding initiating in the fiber. The microstructural failure modes and energy absorption and dissipation properties show strong dependence on the load types, volume fractions and microstructures, with relatively lower dependence on strain rates. For the same microstructure, the stress–strain curve is very sensitive to the strain rate and higher strain rate causes higher stress. The failure mode and the energy absorption and dissipation characteristics mainly depend on the loading type. Materials under compressive loading can absorb more energy than those under shear and tension loadings. For different microstructures, it is found that the composites with 15–20% hexagonal arrangement of fibers provide good designs for energy absorption and dissipation. The micromechanical analysis and results in this paper can be used to develop a homogenized strain-rate dependent constitutive model for rate-dependent deformation and failure in composites under dynamic loading.

#### Acknowledgments

This work has been supported by the Army Research Office through Grant No. DAAD19-02-1-0428 (Program Director: Dr. B. Lamattina) and by the State of Ohio RCP grant. This sponsorship is gratefully acknowledged. Computer support by the Ohio Supercomputer Center through Grant PAS813-2 is also gratefully acknowledged.

#### Appendix A

The coefficients  $A_{ij}$  and  $b_i$  for stress update are given below.

$$\begin{aligned}
A_{11} &= \frac{\partial \phi}{\partial q} + \Delta \varepsilon_{Rp} \left( K \frac{\partial^2 \phi}{\partial p \partial q} + \frac{\partial^2 \phi}{\partial q \partial H^z} \frac{\partial H^z}{\partial \Delta \varepsilon_{Rq}} \right) + \Delta \varepsilon_{Rq} \left( K \frac{\partial^2 \phi}{\partial p^2} + \frac{\partial^2 \phi}{\partial p \partial H^z} \frac{\partial H^z}{\partial \Delta \varepsilon_{Rp}} \right) \\
A_{12} &= \frac{\partial \phi}{\partial p} + \Delta \varepsilon_{Rp} \left( -3G \frac{\partial^2 \phi}{\partial q^2} + \frac{\partial^2 \phi}{\partial q \partial H^z} \frac{\partial H^z}{\partial \Delta \varepsilon_{Rq}} \right) + \Delta \varepsilon_{Rq} \left( -3G \frac{\partial^2 \phi}{\partial p \partial q} + \frac{\partial^2 \phi}{\partial p \partial H^z} \frac{\partial H^z}{\partial \Delta \varepsilon_{Rp}} \right) \\
b_1 &= -\Delta \varepsilon_{Rp} \frac{\partial \phi}{\partial q} - \Delta \varepsilon_{Rq} \frac{\partial \phi}{\partial p} \\
A_{21} &= 1 + \Delta t \left( K \frac{\partial \dot{\lambda}}{\partial p} + \frac{\partial \dot{\lambda}}{\partial H^z} \frac{\partial H^z}{\partial \Delta \varepsilon_{Rp}} \right) \frac{\partial \phi}{\partial p} + \Delta t \dot{\lambda} \left( K \frac{\partial^2 \phi}{\partial p^2} + \frac{\partial^2 \phi}{\partial p \partial H^z} \frac{\partial H^z}{\partial \Delta \varepsilon_{Rp}} \right) \\
A_{22} &= \Delta t \left( -3G \frac{\partial \dot{\lambda}}{\partial q} + \frac{\partial \dot{\lambda}}{\partial H^z} \frac{\partial H^z}{\partial \Delta \varepsilon_{Rq}} \right) \frac{\partial \phi}{\partial p} + \Delta t \dot{\lambda} \left( -3G \frac{\partial^2 \phi}{\partial p \partial q} + \frac{\partial^2 \phi}{\partial p \partial H^z} \frac{\partial H^z}{\partial \Delta \varepsilon_{Rp}} \right) \\
b_2 &= -\Delta \varepsilon_{Rp} - \Delta t \dot{\lambda} \frac{\partial \phi}{\partial p}
\end{aligned} \tag{A.1}$$

where  $H^z$  ( $\alpha = 1, 2, 3$ ) represents the state variables  $\bar{\varepsilon}_M^p$ ,  $f$ , and  $\sigma_0$ .

## References

- ABAQUS, 2005. ABAQUS/Explicit User's Manual, Version 6.5. Providence, Rhode Island, USA.
- Abu Al-Rub, R.K., Voyiadis, G.Z., 2006. A finite strain plastic-damage model for high velocity impact using combined viscosity and gradient localization limiters. Part I – theoretical formulation. *Int. J. Damage Mech.* 15, 293–334.
- Aravas, N., 1987. On the numerical integration of a class of pressure-dependent plasticity models. *Int. J. Numer. Methods Eng.* 24, 1395–1416.
- Austin, R.A., McDowell, D.L., 2011. A dislocation-based constitutive model for viscoplastic deformation of fcc metals at very high strain rates. *Int. J. Plast.* 27, 1–24.
- Bass, J.M., Oden, J.T., 1987. Adaptive finite element methods for a class of evolution problem in viscoplasticity. *Int. J. Eng. Sci.* 25, 623–653.
- Batra, R.C., Hassan, N.M., 2007. Response of fiber reinforced composites to underwater explosive loads. *Compos. Pt. B-Eng.* 38, 448–468.
- Benallal, A., Berstad, T., Borvik, T., Hopperstad, O.S., Koutiri, I., Nogueira de Codes, R., 2008. An experimental and numerical investigation of the behaviour of AA5083 aluminium alloy in presence of the Portevin–Le Chatelier effect. *Int. J. Plast.* 24, 1916–1945.
- Besson, J., Steglich, D., Brocks, W., 2003. Modeling of plane strain ductile rupture. *Int. J. Plast.* 19, 1517–1541.
- Brar, N.S., Joshi, V.S., Harris, B.W., 2009. Constitutive model constants for Al7075-T651 and Al7075-T6. American Physical Society. In: 16th APS Topical Conference on Shock Compression of Condensed Matter.
- Brüning, M., Gerke, S., 2011. Simulation of damage evolution in ductile metals undergoing dynamic loading conditions. *Int. J. Plast.* 27, 1598–1617.
- Carol, I., Rizzi, E., William, K., 1994. A unified theory of elastic degradation and damage based on a loading surface. *Int. J. Solids Struct.* 31, 2835–2865.
- Chaboche, J.L., 1988. Continuum damage mechanics 1. General concepts. *J. Appl. Mech.-Trans. ASME* 55, 59–64.
- Chu, C.C., Needleman, A., 1980. Void nucleation effects in biaxially stretched sheets. *J. Eng. Matl. Tech.* 102, 249–256.
- Clausen, A.H., Børvik, T., Hopperstad, O.S., Benallal, A., 2004. Flow and fracture characteristics of aluminium alloy AA5083-H116 as function of strain rate, temperature and triaxiality. *Mater. Sci. Eng. A-Struct. Mater. Prop. Microstruct. Process.* 364, 260–272.
- Drugan, W.J., Willis, J.R., 1996. A micromechanics-based nonlocal constitutive equation and estimates of representative volume element size for elastic composites. *J. Mech. Phys. Solids* 44, 497–524.
- Farrokh, B., Khan, A.S., 2009. Grain size, strain rate, and temperature dependence of flow stress in ultra-fine grained and nanocrystalline Cu and Al: synthesis, experiment, and constitutive modeling. *Int. J. Plast.* 25, 715–732.
- Farrokh, B., Khan, A.S., 2010. A strain rate dependent yield criterion for isotropic polymers: low to high rates of loading. *Eur. J. Mech. A-Solids* 29, 274–282.
- Fleck, N.A., Hutchinson, J.W., 1993. A phenomenological theory for strain gradient effects in plasticity. *J. Mech. Phys. Solids* 41, 1825–1857.
- Follansbee, P.S., Kocks, U.F., 1988. A constitutive description of the deformation of copper based on the use of the mechanical threshold. *Acta Metall.* 36, 81–93.
- Ghosh, S., Kikuchi, N., 1991. An arbitrary Lagrangian–Eulerian finite element method for large deformation analysis of elastic-viscoplastic solids. *Comput. Method Appl. M.* 86, 127–188.
- Ghosh, S., Bai, J., Paquet, D., 2009. A homogenization based continuum plasticity-damage model for ductile failure of materials containing heterogeneities. *J. Mech. Phys. Solids* 57, 1017–1044.
- Green, A.E., Naghdi, P.M., 1965. A general theory of an elastic–plastic continuum. *Arch. Ration. Mech. An.* 18, 251–281.
- Gurson, A., 1977. Continuum theory of ductile rupture by void nucleation and growth. *J. Eng. Mater. Trans. ASME* 99, 2–15.
- Han, F.S., Zhu, Z.G., Gao, J.C., 1998. Compressive deformation and energy absorbing characteristic of foamed aluminum. *Metall. Mater. Trans. A-Phys. Metall. Mater. Sci.* 29, 2497–2502.
- Hao, S., Brocks, W., 1997. The Gurson–Tvergaard–Needleman-model for rate and temperature-dependent materials with isotropic and kinematic hardening. *Comput. Mech.* 20, 34–40.
- Hu, H.E., Zhen, L., Imai, T., 2010. Strain rate sensitivity of a high strain rate superplastic TiNp/2014 Al composite. *J. Mater. Process. Technol.* 210, 734–740.
- Hwang, K.C., Jiang, H., Huang, Y., Gao, H., Hu, N., 2002. A finite deformation theory of strain gradient plasticity. *J. Mech. Phys. Solids* 50, 81–99.
- Jacinto, A.C., Ambrosini, R.D., Danesi, R.F., 2001. Experimental and computational analysis of plates under air blast loading. *Int. J. Impact Eng.* 25, 927–947.
- Jain, J.R., Ghosh, S., 2009. Damage evolution in composites with a homogenization-based continuum damage mechanics model. *Int. J. Damage Mech.* 18, 533–568.
- Johnson, G.R., Cook, W.H., 1983. A constitutive model and data for metals subjected to large strains, high strain rates and high temperatures. In: *Proceedings of the 7th International Symposium on Ballistics*, pp. 541–547.
- Kachanov, L.M., 1958. Time of the rupture process under creep conditions. *Isv. Akad. Nauk. SSR. Otd. Tekh. Nauk.* 8, 26–31.
- Kanel, G.I., Zaretsky, E.B., Rajendran, A.M., Razorenov, S.V., Savinykh, A.S., Paris, V., 2009. Search for conditions of compressive fracture of hard brittle ceramics at impact loading. *Int. J. Plast.* 25, 649–670.
- Kanit, T., Forest, S., Galliet, I., Mounoury, V., Jeulin, D., 2003. Determination of the size of the representative volume element for random composites: statistical and numerical approach. *Int. J. Solids Struct.* 40, 3647–3679.
- Khan, A.S., Baig, M., 2011. Anisotropic responses, constitutive modeling and the effects of strain-rate and temperature on the formability of an aluminum alloy. *Int. J. Plast.* 27, 522–538.
- Khan, A.S., Farrokh, B., 2006. Thermo-mechanical response of nylon 101 under uniaxial and multi-axial loadings. Part I: experimental results over wide ranges of temperatures and strain rates. *Int. J. Plast.* 22, 1506–1529.

- Khan, A.S., Liang, R.Q., 1999. Behaviors of three BCC metals over wide range of strain rates and temperatures: experiments and modeling. *Int. J. Plast.* 15, 1089–1109.
- Khan, A.S., Suh, Y.S., Kazmi, R., 2004. Quasi-static and dynamic loading responses and constitutive modeling of titanium alloys. *Int. J. Plast.* 20, 2233–2248.
- Khan, A.S., Kazmi, R., Farrokh, B., 2007a. Multiaxial and non-proportional loading responses, anisotropy and modeling of Ti–6Al–4V titanium alloy over wide ranges of strain rates and temperatures. *Int. J. Plast.* 23, 931–950.
- Khan, A.S., Kazmi, R., Farrokh, B., Zupan, M., 2007b. Effect of oxygen content and microstructure on the thermo-mechanical response of three Ti–6Al–4V alloys: experiments and modeling over a wide range of strain-rates and temperatures. *Int. J. Plast.* 23, 1105–1125.
- Kouznetsova, V., Geers, M.G.D., Brekelmans, W.A.M., 2002. Multi-scale constitutive modelling of heterogeneous materials with a gradient-enhanced computational homogenization scheme. *Int. J. Numer. Methods Eng.* 54, 1235–1260.
- Kumar, P., Garg, A., 1988. Failure modes and fractographic study of glass-epoxy composite under dynamic compression. *J. Mater. Sci.* 23, 2305–2309.
- Langdon, G.S., Chung Kim Yuen, S., Nurick, G.N., 2005. Experimental and numerical studies on the response of quadrangular stiffened plates. Part II: localised blast loading. *Int. J. Impact Eng.* 31, 85–111.
- Leblond, J.B., Perrin, G., Suquet, P., 1994. Exact results and approximate models for porous viscoplastic solids. *Int. J. Plast.* 10, 213–235.
- Lee, J., Mal, A., 1998. Characterization of matrix damage in metal matrix composites under transverse loads. *Comput. Mech.* 21, 339–346.
- Lemaitre, J., Chaboche, J.-L., 1990. *Mechanics of Solid Materials*. Cambridge University Press.
- Liang, R., Khan, A.S., 2000. Behaviors of three BCC metals during non-proportional multi-axial loadings and predictions using a recently proposed model. *Int. J. Plast.* 16, 1443–1458.
- Lloyd, D.J., 1994. Particle-reinforced aluminum and magnesium matrix composites. *Int. Mater. Rev.* 39, 1–23.
- Mamalis, A.G., Manolakos, D.E., Ioannidis, M.B., Papapostolou, D.P., 2005. On the response of thin-walled CFRP composite tubular components subjected to static and dynamic axial compressive loading: experimental. *Compos. Struct.*, 69 407–420.
- Meyers, M.A., Andrade, U.R., Chokshi, A.H., 1995. The effect of grain size on the high-strain, high-strain-rate behavior of copper. *Metall. Mater. Trans. A-Phys. Metall. Mater. Sci.* 26, 2881–2893.
- Nahshon, K., Hutchinson, J.W., 2008. Modification of the Gurson model for shear failure. *Eur. J. Mech. A. Solids* 27, 1–17.
- Nahshon, K., Xue, Z., 2009. A modified Gurson model and its application to punch-out experiments. *Eng. Fract. Mech.* 76, 997–1009.
- Nemat-Nasser, S., 1999. Averaging theorems in finite deformation plasticity. *Mech. Mater.* 31, 493–523.
- Nemat-Nasser, S., Choi, J.Y., 2005. Strain rate dependence of deformation mechanisms in a Ni–Ti–Cr shape-memory alloy. *Acta Mater.* 53, 449–454.
- Nemat-Nasser, S., Choi, J.Y., Guo, W.-G., Isaacs, J.B., Taya, M., 2005a. High strain-rate, small strain response of a NiTi shape-memory alloy. *J. Eng. Mater. Technol.* 127, 83–89.
- Nemat-Nasser, S., Choi, J.Y., Guo, W.-G., Isaacs, J.B., 2005b. Very high strain-rate response of a NiTi shape-memory alloy. *Mech. Mater.* 37, 287–298.
- Nemat-Nasser, S., Su, Y., Guo, W.G., Isaacs, J., 2005c. Experimental characterization and micromechanical modeling of superelastic response of a porous NiTi shape-memory alloy. *J. Mech. Phys. Solids* 53, 2320–2346.
- Nemat-Nasser, S., Kang, W.J., McGee, J.D., Guo, W.-G., Isaacs, J.B., 2007. Experimental investigation of energy-absorption characteristics of components of sandwich structures. *Int. J. Impact Eng.* 34, 1119–1146.
- Oguni, K., Ravichandran, G., 2001. Dynamic compressive behavior of unidirectional E-glass/vinylester composites. *J. Mater. Sci.* 36, 831–838.
- Pao, Y.H., Mow, C.C., 1973. *The Diffraction of Elastic Waves and Dynamic Stress Concentrations*. Crane Russak.
- Paquet, D., Ghosh, S., 2010. Microstructural effects on ductile fracture in heterogeneous materials: Part I. sensitivity analysis with LE-VC-FEM. *Eng. Fract. Mech.*
- Pellegrino, C., Galvanetto, U., Schrefler, B.A., 1999. Numerical homogenization of periodic composite materials with non-linear material components. *Int. J. Numer. Methods Eng.* 46, 1609–1637.
- Peng, X., Pi, W., Fan, J., 2008. A microstructure-based constitutive model for the pseudoelastic behavior of NiTi SMAs. *Int. J. Plast.* 24, 966–990.
- Preston, D.L., Tonks, D.L., Wallace, D.C., 2003. Model of plastic deformation for extreme loading conditions. *J. Appl. Phys.* 93, 211–220.
- Rao, K.T.V., Siu, S.C., Ritchie, R.O., 1993. Failure mechanisms in SiC-fiber reinforced 6061 aluminum alloy composites under monotonic and cyclic loading. *Metall. Mater. Trans. A-Phys. Metall. Mater. Sci.* 24, 721–734.
- Segurado, J., Llorca, J., 2002. A numerical approximation to the elastic properties of sphere-reinforced composites. *J. Mech. Phys. Solids* 50, 2107–2121.
- Shalu, T., Abhilash, E., Joseph, M.A., 2009. Development and characterization of liquid carbon fibre reinforced aluminium matrix composite. *J. Mater. Process. Technol.* 209, 4809–4813.
- Simo, J.C., Ju, J.W., 1987. Strain- and stress-based continuum damage models-I. Formulation. *Int. J. Solids Struct.* 23, 821–840.
- Specialty Materials Inc., 2010. <<http://www.specmaterials.com/>>.
- Steinberg, D.J., Lund, C.M., 1988. A constitutive model for strain rates from  $10^{-4}$  to  $10^6 \text{ s}^{-1}$ . *Journal de physique. Colloques* 49, 3–3.
- Steinberg, D.J., Cochran, S.G., Guinan, M.W., 1980. A constitutive model for metals applicable at high-strain rate. *J. Appl. Phys.* 51, 1498–1504.
- Swaminathan, S., Ghosh, S., 2006. Statistically equivalent representative volume elements for composite microstructures. Part II: with damage. *J. Comput. Mater.* 40 (7), 605–621.
- Swaminathan, S., Ghosh, S., Pagano, N.J., 2006. Statistically equivalent representative volume elements for composite microstructures. Part I: without damage. *J. Comput. Mater.* 40 (7), 583–604.
- Tvergaard, V., 1981. Influence of voids on shear band instabilities under plain strain conditions. *Int. J. Fract.* 17, 389–407.
- Tvergaard, V., 1982. On localization in ductile materials containing spherical voids. *Int. J. Fract.* 18, 237–252.
- Tvergaard, V., 1990. Material failure by void growth to coalescence. *Adv. Appl. Mech.* 27, 83–151.
- Tvergaard, V., Needleman, A., 1984. Analysis of cup-cone fracture in a round tensile bar. *Acta Metall.* 32, 157–169.
- Tvergaard, V., Needleman, A., 1995. Effect of nonlocal damage in porous plastic solids. *Int. J. Solids Struct.* 32, 1063–1077.
- Valiev, R.Z., Salimonenko, D.A., Tsenev, N.K., Berbon, P.B., Langdon, T.G., 1997. Observations of high strain rate superplasticity in commercial aluminum alloys with ultrafine grain sizes. *Scripta. Mater.* 37, 1945–1950.
- Voyiadjis, G.Z., Abu Al-Rub, R.K., 2006. A finite strain plastic-damage model for high velocity impact using combined viscosity and gradient localization limiters. Part II: numerical aspects and simulation. *Int. J. Damage Mech.* 15, 335–373.
- Wen, J., Huang, Y., Hwang, K.C., Liu, C., Li, M., 2005. The modified Gurson model accounting for the void size effect. *Int. J. Plast.* 21, 381–395.
- Wu, C.T., Koishi, M., 2009. A meshfree procedure for the microscopic analysis of particle-reinforced rubber compounds. *Interact. Multiscale Mech.* 2, 147–169.
- Xue, Z., Pontin, M.G., Zok, F.W., Hutchinson, J.W., 2010. Calibration procedures for a computational model of ductile fracture. *Eng. Fract. Mech.* 77, 492–509.
- Zerilli, F.J., Armstrong, R.W., 1987. Dislocation-mechanics-based constitutive relations for material dynamics calculations. *J. Appl. Phys.* 61, 1816–1825.
- Zhou, Y., Mahfuz, H., Jeelani, S., 2005. Numerical simulation for high strain rate failure process of unidirectional SiC-Al composites. *Int. J. Damage Mech.* 14, 321–341.